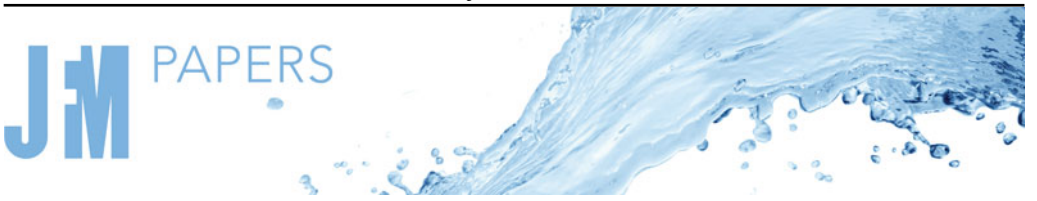
J. Fluid Mech. (2026), *vol.* 1042, A13, doi:10.1017/jfm.2026.11820



A novel multiscale model for the haemodynamics in retinal microcirculation with an analytic solution for the capillary–tissue coupled system

Chang Lin[1], **Zilong Song**[2], **Robert S. Eisenberg**[3], **Shixin Xu**[4] and **Huaxiong Huang**[4]

[1]School of Mathematical Sciences, Beijing Normal University, Beijing, PR China

[2]Department of Mathematics and Statistics, Utah State University, Logan, UT, USA

[3]Department of Applied Mathematics, Illinois Institute of Technology, Chicago, IL, USA

[4]Zu Chongzhi Centre, Duke Kunshan University, Kunshan, PR China

Corresponding author: Huaxiong Huang, hhuang@yorku.ca

(Received 26 November 2025 UTC; revised 11 June 2026 UTC; accepted 17 June 2026 UTC)

Mathematical modelling of the microcirculatory haemodynamics in the retina is an essential tool for understanding various diseases of the retina, yet remains challenging due to the multiscale nature of the retinal vasculature and its coupling to surrounding tissue. To address this, we develop a multiscale model that couples retinal vasculature across scales with interstitial tissue. Our model combines the one-dimensional model for arterioles and venules with the coupled Darcy equations for capillaries and tissue. The model uses an analytic solution for the capillary–tissue coupled system that provides a simple interpretation of the results along with much faster computation. The analytic solution implies a dynamic coupling condition that links the capillary bed with upstream arteriolar and downstream venular flows. The model is mathematically robust, demonstrated through analysis of the solution's truncation error and convergence. Its predictive accuracy is validated against experimental data and other models, making it useful in interpreting experimental results. Finally, the role of various parameters in controlling retinal haemodynamics is explored.

Key words: biological fluid dynamics, biomedical flows, blood flow

1. Introduction

The retina is a thin and multilayered neural tissue lining the back of the eye that plays a crucial role in visual function. Its function depends sensitively on adequate blood supply, as retinal haemodynamics helps sustain the metabolism that keeps the retina

© The Author(s), 2026. Published by Cambridge University Press.

https://doi.org/10.1017/jfm.2026.11820 Published online by Cambridge University Press

alive and functional (Kornfield & Newman 2015). Disruptions in the haemodynamics can impair oxygen and nutrient delivery, contributing to various retinopathies such as diabetic retinopathy (Kornfield & Newman 2015), glaucoma (Garhöfer *et al.* 2004; Caprioli & Coleman 2010; Ch'ng *et al.* 2021) and retinal vascular occlusion (Osborne *et al.* 2004). Understanding retinal haemodynamics is thus essential for understanding the life of the retina in health and disease.

Computational modelling serves as a crucial and powerful tool for exploring the retinal haemodynamics, integrating physiological processes that are difficult to measure *in vivo* (Siggers & Ethier 2012; Ruffini *et al.* 2024). Different models have been employed in retinal haemodynamics and oxygenation. Lumped parameter zero-dimensional (0-D) models, representing the vasculature as a hydraulic resistor circuit (Flores *et al.* 2016), have helped to resolve the inconsistencies in clinical data (Guidoboni *et al.* 2014*b*). The 0-D lumped model is also exploited in the simulation of retinal circulation (Ganesan *et al.* 2010; Fry *et al.* 2018). More complicated models, including a one-dimensional (1-D) model, two-dimensional (2-D) model and three-dimensional (3-D) model, have been used to reveal fundamental properties of oxygen transport in the retina (Liu *et al.* 2009; Causin *et al.* 2016) as well as deal with properties of disease in specific patients (Malek *et al.* 2015; Rebhan *et al.* 2019; Julien *et al.* 2023; Tripathy *et al.* 2023). Existing models provide valuable physiological and pathological insights, however, they focus on specific vascular compartments, including simplifications such as constant capillary pressure or neglecting interactions between capillaries and surrounding tissue. Consequently, very few existing models combine the arterioles, venules, capillaries and tissue equally into a comprehensive model. In other tissues, the general rule that all compartments interact with each other has required a systematic structural analysis of flow (Eisenberg 2023), and the same should hold true for the retina.

A central challenge in modelling the haemodynamics of retinal microcirculation stems from intrinsic multiscale vasculature. Arteriolar and venular networks display hierarchical tree-like branching (Julien *et al.* 2023), while capillaries form an interconnected mesh-like structure (Fry *et al.* 2018; Shipley *et al.* 2019). Thus, retinal microcirculation inherently constitutes a multiscale system, involving small-scale details of flow inside blood vessels and also the large-scale layout of the blood vessels. These issues can be addressed using existing methodologies for other organs or tissues, including tumour perfusion (d'Esposito *et al.* 2018), transport in breast tissue (Fritz *et al.* 2022) and microcirculatory haemodynamics (Shipley *et al.* 2019; Sweeney *et al.* 2024), where a continuum Darcy model for capillary flow is typically coupled to arterial and venous trees via point sources. Even with the point source approximation, the computation is challenging because the Darcy model has to be solved simultaneously with arterial and venous flows (Qohar *et al.* 2021; Fritz *et al.* 2022). A novel alternative is to use the analytic solution for the capillary flow, which expresses the pressure explicitly so that the Darcy model does not have to be solved in the entire domain. The analytical solution provides significant physical insight as well as much faster computation (d'Esposito *et al.* 2018; Shipley *et al.* 2019; Sweeney *et al.* 2024). However, in current analytic methods the fluid exchange between capillaries and tissue is treated approximately. They describe the coupling of capillaries between surrounding tissues using a far-field boundary condition. While this serves as a reasonable first step, it does not capture the local fluid exchange between these two components, and a more realistic description should include such exchange.

Our work complements previous studies by developing a novel multiscale model that fully couples retinal vasculature with interstitial tissue. Specifically, the flows in arterioles and venules are described by a 1-D model (Julien *et al.* 2023), while capillaries and surrounding tissue are treated as two coupled porous media and the flow in them is

https://doi.org/10.1017/jfm.2026.11820 Published online by Cambridge University Press

described by the Darcy equation. The fluid exchange between the capillary and tissue is modelled by the source/sink of the two Darcy equations, one for capillary (drainage) and the other for the tissue (feed). Moreover, the vasculature is coupled as follows. Terminal arterioles/venules in the superficial layer act as point sources/sinks in the capillary Darcy equation, and the pressure difference between these vessels and the capillary network is related to the flow rates at point sources/sinks by the effective resistors in the deep layer, which provides the outlet/inlet boundary condition for the arteriolar/venular tree in the superficial layer. What further distinguishes our modelling from others is the analytic solution for the capillary–tissue system, which is derived on a finite domain with physiological boundary conditions. We analyse the convergence and truncation error of the analytical solution extensively to ensure its robustness and accuracy. The analysis of the solution's convergence also reveals some interesting properties, which might suggest a new modelling methodology for other tissues. The model is validated against experimental data and the results from existing models, and pulsatile pressures within arterioles and venules are also simulated. Moreover, we demonstrate our model's capability by exploring the effects of parameter variations.

The rest of the paper is organised as follows. In § 2 we describe the models for vasculature and surrounding tissue, including the 1-D model for arterioles and venules, the synthetic vascular network model and the continuum formulation for the capillary–tissue system. In § 3, we derive the analytic solution of capillary–tissue coupled system, and its convergence is analysed. In § 4, the numerical methods for the proposed model are described, and multiple simulations are performed to assess the model's accuracy and demonstrate its capability in § 5. The sensitivity of various parameters is explored in § 6. Section 7 consists of the conclusion and discussion.

2. Models

2.1. *Network-based simulation for arteriolar and venular trees*

2.1.1. *One-dimensional model*

The 1-D model is widely adopted to describe the blood flow in the individual vessels of arteriolar and venular networks. The networks exist in 3-D space but are often analysed in a 2-D subset of 3-D space following the usual conventions of electric circuit theory. For all time $t > 0$, the flow within each vessel is characterised by the flow rate $q(s, t)$ and the cross-sectional area $A(s, t)$ (Wang *et al.* 2016; Julien *et al.* 2023), along the axis s of the vessel, and their evolutions are given by

$$\begin{cases} \dfrac{\partial A}{\partial t} + \dfrac{\partial q}{\partial s} = 0, \\ \dfrac{\partial q}{\partial t} + \dfrac{\partial}{\partial s}\left(\hat{\alpha}\dfrac{q^2}{A}\right) + \dfrac{A}{\rho}\dfrac{\partial p}{\partial s} = C_f, \end{cases} \tag{2.1}$$

where $\hat{\alpha}$ is the coefficient (momentum flux correction factor) that describes the velocity profile in each vessel (Müller & Toro 2014), p is the pressure, ρ is the density of blood and C_f is the friction term. The coefficient $\hat{\alpha}$ is set as $\hat{\alpha} = 4/3$, which corresponds to a parabolic velocity profile that is consistent with the experimental data in the retina (Song *et al.* 2014; Kornfield & Newman 2015; Causin *et al.* 2016). The density is set as $\rho = 1\ \mathrm{g\,cm^{-3}}$ from now on in this paper. The explicit form of friction term is given by

https://doi.org/10.1017/jfm.2026.11820 Published online by Cambridge University Press

(Audebert *et al.* 2017; Liu & Suito 2024)

$$C_f = \begin{cases} -8\pi \dfrac{\eta}{\rho}\dfrac{q}{A}, & \text{for arterioles,} \\ -8\pi \sqrt{\dfrac{A}{A_0}}\dfrac{\eta}{\rho}\dfrac{q}{A}, & \text{for venules,} \end{cases} \tag{2.2}$$

where $\eta = \eta(r)$ is the apparent viscosity, modelled as a function of the vessel radius r to account for the rheological properties of blood.

The fluid–structure interaction in the problem is captured by the following elastic model (Müller & Toro 2014; Liu & Suito 2024):

$$p - p_{ext} = K\left[\left(\frac{A}{A_0}\right)^{\beta_1} - \left(\frac{A}{A_0}\right)^{\beta_2}\right], \tag{2.3}$$

where p_{ext} is the exterior pressure, K is the rigidity, β_1 and β_2 are parameters depending on the vessel wall behaviour and A_0 is the neutral area of the vessel, which differs for each vessel. The values of K, β_1 and β_2 vary with the vessel position and its function. The rigidity is

$$K = \begin{cases} \dfrac{4}{3}\dfrac{\pi^{1/2}Eh}{A_0^{1/2}}, & \text{for arterioles,} \\ \dfrac{1}{9}\dfrac{\pi^{3/2}Eh^3}{A_0^{3/2}}, & \text{for venules,} \end{cases} \tag{2.4}$$

where E is the Young's modulus and h is the thickness of the vessel wall. The parameters β_1 and β_2 are given by

$$\beta_1 = \begin{cases} 1/2, & \text{for arterioles,} \\ 10, & \text{for venules,} \end{cases} \tag{2.5}$$

and

$$\beta_2 = \begin{cases} 0, & \text{for arterioles,} \\ -3/2, & \text{for venules.} \end{cases} \tag{2.6}$$

The expression of K and values of β_1 and β_2 for arterioles are mainly taken from previous work on modelling of arteriolar circulation (Julien *et al.* 2023), while those for venules are adopted from the model of veins in other tissues (Müller & Toro 2014; Audebert *et al.* 2017). The values of E for arterioles and venules are set to the same value as a reasonable approximation (Julien *et al.* 2023). The wall thickness h is proportional to the vessel diameter, which is given by $h = \mathrm{WLR} \times 2r_0$, where WLR is the wall-to-lumen ratio and r_0 is the radius of neutral area A_0. For arterioles, the value of WLR is based on experimental observations (Arichika *et al.* 2015), while for venules, a smaller value is employed to account for their thinner walls. Values of parameters in 1-D model are summarised in table 1.

The apparent viscosity of blood decreases strongly with the decreasing vessel radius from approximately 150 to approximately 5 μm, then increases below 5 μm. This unique rheological behaviour is the Fåhræus–Lindqvist effect. To characterise blood's rheological properties, we use an empirical relation developed by Pries *et al.* that expresses viscosity

https://doi.org/10.1017/jfm.2026.11820 Published online by Cambridge University Press

Parameter	Value	References
Viscosity model		
η_p	1.2 cP	Pries *et al.* (1994) Secomb & Pries (2013) Bappoo *et al.* (2017)
Elastic model		
E	10^6 g cm^{-1} s^{-2}	Julien *et al.* (2023) Ferrara *et al.* (2021)
WLR	0.16 (arteriole) 0.12 (venule)	Arichika *et al.* (2015) Ertop *et al.* (2023)
IOP	16 mmHg	Guidoboni *et al.* (2014*b*)
L-system		
Diameter of CRA	165 ± 15 µm	Dorner *et al.* (2002) Brown *et al.* (2024) Hernandez *et al.* (2024)
Diameter of CRV	196 ± 15 µm	Riva *et al.* (1985)
ξ	36 ± 6	Brown *et al.* (2024)
v_a	1 ($d_v > 50$ µm) 0.8 ($d_v \leq 50$ µm)	Brown *et al.* (2024)
γ	2.1 ($d_v > 50$ µm) 2 ($d_v \leq 50$ µm)	Brown *et al.* (2024)
Structured tree model		
ξ	23	Liu *et al.* (2009) Julien *et al.* (2023)
v_a	0.8	Brown *et al.* (2024) Liu *et al.* (2009)
γ	2	Julien *et al.* (2023)
Capillary–tissue coupled system		
μ_{cap}	Computed by the viscosity model	Pries *et al.* (1994)
μ_t	0.7 cP	Estimated
R_t	1.6 cm	Causin *et al.* (2016)
α_r	1	Truskey *et al.* (2009)
$\Delta\pi$	16 mmHg	Morissette (1977)
Boundary conditions at CRA and CRV		
$p_{in,CRA}$ (steady)	62 mmHg	Guidoboni *et al.* (2014*b*)
$p_{in,CRA}$ (pulsatile)	$45 - 77$ mmHg	Rebhan *et al.* (2019) Guidoboni *et al.* (2014*b*)
$p_{out,CRV}$	16 mmHg	Rebhan *et al.* (2019) Causin *et al.* (2016) Guidoboni *et al.* (2014*a*)

Table 1. Parameters for the haemodynamics in retinal microcirculation.

as a function of vessel radius (Pries *et al.* 1994; Secomb & Pries 2013; Bappoo *et al.* 2017)

$$\eta(r) = \eta_p \left[1 + (\eta_{45} - 1) \left(\frac{r}{r - 0.55} \right)^2 \right] \left(\frac{r}{r - 0.55} \right)^2, \tag{2.7}$$

where r is the vessel radius (in unit µm), η_p is the viscosity of plasma set as $\eta_p = 0.012$ Poise and η_{45} is the relative apparent blood viscosity for discharge haematocrit

https://doi.org/10.1017/jfm.2026.11820 Published online by Cambridge University Press

of 0.45 given by

$$\eta_{45} = 6\exp(-0.17r) + 3.2 - 2.44\exp\left[-0.06(2r)^{0.645}\right]. \tag{2.8}$$

Note that the 1-D model is adopted for superficial vessels, which are visible in fundus images. As a result, the external pressure acting on the vessel walls is approximately the intraocular pressure (IOP) (Kiel 2011), and thus in the 1-D model, external pressure is set to $p_{ext} = \text{IOP}$. A similar approximation is employed in previous work (Guidoboni *et al.* 2014*b*). Smaller vessels are distributed in the deep layer and invisible in fundus images, which makes them difficult to distinguish clinically. The standard method is to model these deep vessels as effective resistors that connect the superficial vascular trees to the capillary bed. The synthetic vascular network model for both superficial and deep vessels is described below.

2.1.2. *Synthetic vascular network model*

Next, we construct a network from individual vessels. We exploit a Lindenmayer system (L-system) to generate synthetic arteriolar and venular trees in the superficial layer (Brown *et al.* 2024). The vasculature begins with the central retinal artery (CRA) and central retinal vein (CRV), which are perpendicular to the tissue at the centre of the optic disc. Branches are added iteratively and asymmetrically to create bifurcations up to the fifth generation, with lengths given by $l_v = \xi r_v$, where ξ is the length-to-radius ratio and r_v is the vessel radius. At each bifurcation boundary one mother vessel is connected to two daughter vessels, and two branching angles θ_{d_1} and θ_{d_2} are determined by (Zamir 2001; Brown *et al.* 2024)

$$\cos\theta_{d_1} = \frac{(1+v_a^3)^{4/3} + v_a^4 - 1}{2v_a^2(1+v_a^3)^{2/3}}, \tag{2.9}$$

$$\cos\theta_{d_2} = \frac{(1+v_a^3)^{4/3} + 1 - v_a^4}{2v_a^2(1+v_a^3)^{2/3}}, \tag{2.10}$$

where $v_a = r_{d_2}/r_{d_1} < 1$ is the asymmetry ratio, with radii r_{d_1} and r_{d_2} of two daughter vessels, and normally distributed noise is added to branching angle values with a standard deviation of $\pi/36$. The vessel radii follow an asymmetric branching relation

$$r_M^\gamma = r_{d_1}^\gamma + r_{d_2}^\gamma, \tag{2.11}$$

where r_M is the radius of the mother vessel and γ is the junction exponent (Zamir 2001; Brown *et al.* 2024). Given the radius of the root vessel r_M and the value of v_a, radii of two daughter vessels are determined by (Zamir 2001; Liu *et al.* 2009)

$$r_{d_1} = (1+v_a^\gamma)^{-1/\gamma} r_M, \tag{2.12}$$

$$r_{d_2} = v_a(1+v_a^\gamma)^{-1/\gamma} r_M. \tag{2.13}$$

Generated vascular trees are shown in figure 1(*a*), where the arteriolar tree is displayed in red and venular tree is displayed in blue. For comparison, a real retinal vasculature from the DRIVE dataset (Staal *et al.* 2004) and its manual segmentation are shown in figures 1(*b*) and 1(*c*), respectively.

Arterioles and venules in deep layer are constructed using a structured tree model to set the resistive boundary condition for the vascular trees in the superficial layer (Liu *et al.* 2009; Malek *et al.* 2015; Julien *et al.* 2023). This boundary condition is defined by the

https://doi.org/10.1017/jfm.2026.11820 Published online by Cambridge University Press

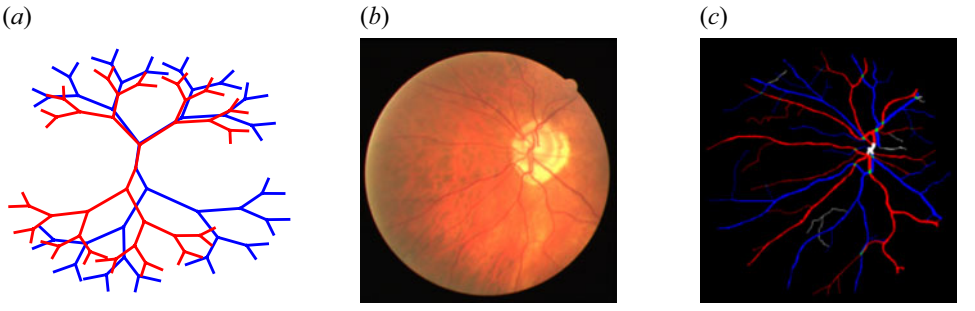


Figure 1. Synthetic and real retinal vasculature. (*a*) The arteriolar (red) and venular (blue) trees in retinal tissue generated using an L-system. (*b*) Fundus image from the DRIVE dataset (Staal *et al.* 2004). (*c*) The manually segmented retinal vasculature for (*b*). Arterioles and venules are displayed in red and blue, respectively. The green denotes pixels classified as both arteriole and venule and the white denotes the uncertain segment.

Poiseuille equation for steady, viscous flow, which describes the relation between flow and pressure, given by

$$p_{up} - p_{down} = Rq, \tag{2.14}$$

where p_{up} and p_{down} are the upstream and downstream pressures, R is the resistance and q is flow rate.

In the structured tree model deep vessels grow from terminal superficial vessels until their radii are decreased to $r = 6\,\mu\text{m}$, which is the characteristic radius of the capillary (Józsa *et al.* 2021; Fritz *et al.* 2022), and the branching is performed similarly to that in the L-system (Julien *et al.* 2023). The radius of vessel r_v is computed using (2.12) or (2.13), while the length is given by $l_v = \xi r_v$. Given the radius and length, the resistance of a single vessel is given by

$$R_k = \frac{8\eta_k l_k}{\pi r_k^4}, \tag{2.15}$$

where the viscosity η_k is computed using Pries *et al.*'s model. Then the equivalent resistance of the root vessel in a structured tree is calculated recursively for the resistive boundary condition. For a vessel M with its own resistance R_M and its daughter vessels with resistances $R_{d_1,eq}$ and $R_{d_2,eq}$, the total equivalent resistance is

$$R_{M,eq} = R_M + R_{d,eq}, \tag{2.16}$$

where

$$\frac{1}{R_{d,eq}} = \frac{1}{R_{d_1,eq}} + \frac{1}{R_{d_2,eq}}. \tag{2.17}$$

2.2. *Continuum formulation for the capillary network and surrounding tissue*

2.2.1. *Physiological basis and modelling simplification*

In our model we treat the retina as a porous medium, given its composition of cells, fibres and interstitial space filled with a fluid. The capillary bed forms multiple interconnected plexuses: the superficial, intermediate and deep plexuses, rather than a collection of a few discrete, isolated branches. These plexuses are densely distributed in the neural tissue, and they are compressed into a single porous medium so that the essential haemodynamics could be effectively described. Given bidirectional fluid exchange between capillaries and surrounding tissue, these two systems should be combined in the same way that electrical

https://doi.org/10.1017/jfm.2026.11820 Published online by Cambridge University Press

systems are combined in electrical models of syncytial tissue (Eisenberg 2023). We thus model the capillary bed and surrounding tissue as interacting porous media.

2.2.2. *Capillary–tissue coupled system*

The flow in both the capillary bed and surrounding tissue is modelled as a Darcy flow (Shipley *et al.* 2019; Qohar *et al.* 2021; Fritz *et al.* 2022; Sweeney *et al.* 2024). The Darcy flux of capillaries $\boldsymbol{u}_{cap}$, i.e. volumetric flow rate per unit area (in unit cm s^{-1}), is given by

$$\boldsymbol{u}_{cap} = -\frac{1}{\mu_{cap}} \boldsymbol{k}_{cap} \cdot \boldsymbol{\nabla} p_{cap} \quad \text{in} \quad \Omega_t, \tag{2.18}$$

where $\boldsymbol{k}_{cap}$ is the permeability tensor (in unit μm^2), μ_{cap} is the viscosity of blood and p_{cap} is the pressure of capillary network. Equation (2.18) states that the flow in capillaries is mainly driven by the pressure gradient, which is consistent with flow characteristics in retinal vasculature physiologically. The capillary network is assumed isotropic and homogeneous (Vidotto *et al.* 2019; Qohar *et al.* 2021) such that the permeability tensor is $\boldsymbol{k}_{cap} = k_{cap}\boldsymbol{I}$, where $\boldsymbol{I}$ is the identity matrix. Since the blood is incompressible, conservation of mass yields

$$\boldsymbol{\nabla} \cdot \boldsymbol{u}_{cap} = \psi_{cap} \quad \text{in} \quad \Omega_t, \tag{2.19}$$

where ψ_{cap} is the source term (in unit s^{-1}). Combining (2.18) and (2.19), the flow in capillaries is characterised by the following equation:

$$-\frac{k_{cap}}{\mu_{cap}} \nabla^2 p_{cap} = \psi_{cap}(\boldsymbol{x}) \quad \text{in} \quad \Omega_t. \tag{2.20}$$

The source term should combine three key components: arteriolar inflow, venular drainage and the fluid exchange between capillaries and surrounding tissue, which is expressed as

$$\psi_{cap}(\boldsymbol{x}) = \psi_{ac} + \psi_{cv} - \psi_{ct}, \tag{2.21}$$

where ψ_{ac}, ψ_{cv} and ψ_{ct} denote arteriolar inflow, venular drainage and fluid exchange between capillaries and the tissue, respectively. The contributions of arteriolar and venular trees are modelled as the summation of discrete point sources

$$\psi_{ac}(\boldsymbol{x}) + \psi_{cv}(\boldsymbol{x}) = \sum_{n=1}^{N_{cap}} q_n \delta(\boldsymbol{x} - \boldsymbol{x}_n), \tag{2.22}$$

where N_{cap} is the total number of point sources, q_n represents the flow rate of source/sink at location $\boldsymbol{x}_n$ and $\delta(\cdot)$ is the Dirac delta function. The fluid exchange between capillaries and tissue is mainly determined by their hydrostatic and osmotic pressures. Using Starling's filtration principle, the fluid filtration rate is given by (Xu *et al.* 2018; Vidotto *et al.* 2019; Fritz *et al.* 2022)

$$\psi_{ct}(\boldsymbol{x}) = L_h \times S \times [(p_{cap}(\boldsymbol{x}) - p_t(\boldsymbol{x})) - \alpha_r(\pi_{cap}(\boldsymbol{x}) - \pi_t(\boldsymbol{x}))], \tag{2.23}$$

where L_h is the hydraulic conductivity of the capillary wall, S is the capillary surface area per unit volume of tissue, p_t is the tissue pressure in retinal layers, π_{cap} is the capillary plasma osmotic pressure, π_t is the interstitial fluid osmotic pressure and α_r is the permeability of the capillary wall to proteins. Due to the tight junctions of the blood–retinal barrier (BRB), the capillary wall is largely impermeable to plasma proteins, which implies that $\alpha_r \approx 1$ under normal physiological conditions (Truskey *et al.* 2009). For our

https://doi.org/10.1017/jfm.2026.11820 Published online by Cambridge University Press

model focusing on the haemodynamics, the osmotic pressure difference $\Delta\pi = \pi_{cap} - \pi_t$ is treated as a constant. This is reasonable when the protein leakage is minimal and capillary protein concentrations do not vary dramatically along the vascular network, consistent with our continuum-scale averaging over capillaries. The source ψ_{ct} can be written as

$$\psi_{ct}(\boldsymbol{x}) = \alpha_{exch} \times (p_{cap}(\boldsymbol{x}) - p_t(\boldsymbol{x}) - \alpha_r \Delta\pi), \tag{2.24}$$

where $\alpha_{exch} = L_h \times S$ is the fluid exchange rate (in unit $\mu\mathrm{m\,s\,g^{-1}}$). Similarly, the tissue pressure satisfies

$$-\frac{k_t}{\mu_t}\nabla^2 p_t = \psi_{ct}, \quad \text{in} \quad \Omega_t, \tag{2.25}$$

where k_t is the permeability for the interstitial fluid in tissue and μ_t is the viscosity of interstitial fluid in tissue. Note that active pumping of retinal pigment epithelium and passive exchange with the vitreous chamber and choroid (Dvoriashyna *et al.* 2018; Ruffini *et al.* 2024) are not included, since these mechanisms mainly regulate long-term fluid homeostasis and baseline pressure, rather than the local pressure differences that drive capillary–tissue exchange. Then the coupled system for capillary and interstitial fluid pressure is given by

$$\begin{cases} -\dfrac{k_{cap}}{\mu_{cap}}\nabla^2 p_{cap} = \displaystyle\sum_{n=1}^{N_{cap}} q_n \delta(\boldsymbol{x} - \boldsymbol{x}_n) - \alpha_{exch}(p_{cap} - p_t - \alpha_r \Delta\pi) \quad \text{in} \quad \Omega_t, \\ -\dfrac{k_t}{\mu_t}\nabla^2 p_t = \alpha_{exch}(p_{cap} - p_t - \alpha_r \Delta\pi) \quad \text{in} \quad \Omega_t. \end{cases} \tag{2.26}$$

Previous studies usually assume an idealised geometry of the tissue domain Ω_t, such as a sphere (Siggers & Ethier 2012; Rebhan *et al.* 2019; Tripathy *et al.* 2023), a circular domain with radial cuts (Ganesan *et al.* 2010; Fry *et al.* 2018) or an equivalent rectangle with the same area (Causin *et al.* 2016), which is motivated by the spherical anatomy of the retina. Following this precedent, we assume a circular domain of radius R_t for the tissue.

2.2.3. *Boundary conditions*

We next specify the boundary conditions for capillary and tissue pressures. Physiologically, blood does not flow across the boundary $\partial\Omega_t$. Since the flux of blood across the boundary is described by $-(k_{cap}/\mu_{cap})\nabla p_{cap} \cdot \boldsymbol{n}$, enforcing this flux to be zero implies the following boundary condition for p_{cap}

$$-\frac{k_{cap}}{\mu_{cap}}\nabla p_{cap} \cdot \boldsymbol{n} = 0 \quad \text{on} \quad \partial\Omega_t. \tag{2.27}$$

For the tissue pressure, since all fluid exchanges are included in the source, the flux of interstitial fluid on the boundary is zero, and thus the boundary condition for tissue pressure is given by

$$-\frac{k_t}{\mu_t}\nabla p_t \cdot \boldsymbol{n} = 0 \quad \text{on} \quad \partial\Omega_t. \tag{2.28}$$

https://doi.org/10.1017/jfm.2026.11820 Published online by Cambridge University Press

Moreover, these two boundary conditions correspond to two fundamental conservation laws. First, integrating the boundary condition for p_t over $\partial\Omega_t$ yields

$$\int_{\partial\Omega_t} -\frac{k_t}{\mu_t}\nabla p_t \cdot \boldsymbol{n}\mathrm{d}s = \int_{\Omega_t} -\frac{k_t}{\mu_t}\nabla^2 p_t \mathrm{d}\boldsymbol{x} = \int_{\Omega_t} \alpha_{exch}(p_{cap} - p_t - \alpha_r \Delta\pi)\mathrm{d}\boldsymbol{x} = 0, \tag{2.29}$$

which implies that

$$\int_{\Omega_t} p_{cap}\mathrm{d}\boldsymbol{x} = \int_{\Omega_t} p_t \mathrm{d}\boldsymbol{x} + \alpha_r \int_{\Omega_t \Delta\pi \mathrm{d}\boldsymbol{x}}. \tag{2.30}$$

This equality states the tissue fluid homeostasis, where the integrated capillary and interstitial fluid pressures are balanced by the oncotic pressure difference, ensuring that no pathological fluid accumulation occurs in the interstitium. Second, integrating the boundary condition for p_{cap} implies

$$\begin{aligned}\int_{\partial\Omega_t} -\frac{k_{cap}}{\mu_{cap}}\nabla p_{cap} \cdot \boldsymbol{n}\mathrm{d}s &= \int_{\Omega_t} \psi_{cap}\mathrm{d}\boldsymbol{x} \\ &= \sum_{n=1}^{N_{cap}} q_n - \int_{\Omega_t} \alpha_{exch}(p_{cap} - p_t - \alpha_r\Delta\pi)\mathrm{d}\boldsymbol{x},\end{aligned} \tag{2.31}$$

thus the boundary condition that $-(k_{cap}/\mu_{cap})\nabla p_{cap} \cdot \boldsymbol{n} = 0$ is satisfied only if $\sum_{n=1}^{N_{cap}} q_n = 0$, which states the conservation of mass.

2.3. *Boundary conditions for vascular tree and multiscale coupling*

It remains to specify the boundary conditions for the 1-D model, as well as the coupling conditions at the interfaces where arterioles and venules connect to the capillaries.

The pressure boundary conditions are imposed at the CRA inlet and the CRV outlet. While the pressure at the CRA could be constant or time-dependent, that at CRV outlet is set to be constant. We denote the areas at the CRA inlet and the CRV outlet as $A_{in,CRA}$ and $A_{out,CRV}$, respectively. The area $A_{in,CRA}$ is determined by solving the equation

$$p_{in,CRA} - p_{ext} = K\left[\left(\frac{A_{in,CRA}}{A_0}\right)^{\beta_1} - \left(\frac{A_{in,CRA}}{A_0}\right)^{\beta_2}\right], \tag{2.32}$$

where $p_{in,CRA}$ is the prescribed pressure at CRA inlet, and the corresponding flow rate $q_{in,CRA}$ is obtained from the mass-conservation equation

$$\frac{\partial A_{CRA}}{\partial t} + \frac{\partial q_{CRA}}{\partial s} = 0. \tag{2.33}$$

Similarly, the area $A_{out,CRV}$ is computed from

$$p_{out,CRV} - p_{ext} = K\left[\left(\frac{A_{out,CRV}}{A_0}\right)^{\beta_1} - \left(\frac{A_{out,CRV}}{A_0}\right)^{\beta_2}\right], \tag{2.34}$$

where $p_{out,CRV}$ is the prescribed pressure at CRV outlet. At CRV outlet, constant pressure implies a constant area $A_{out,CRV}$, and the mass-conservation equation then yields the boundary condition that $\partial q/\partial s = 0$. The bifurcation boundary conditions are governed

https://doi.org/10.1017/jfm.2026.11820 Published online by Cambridge University Press

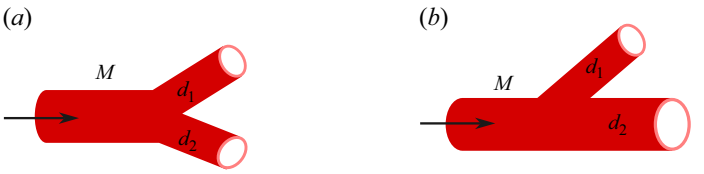


Figure 2. Two different bifurcation boundaries.

by the following equations (Köppl & Helmig 2023):

$$\begin{cases} q_M - q_{d_1} - q_{d_2} = 0, \\ p_M - p_{d_1} = 0, \\ p_M - p_{d_2} = 0, \\ \dfrac{\partial A_M}{\partial t} + \dfrac{\partial q_M}{\partial s_M} = 0, \\ \dfrac{\partial A_{d_1}}{\partial t} + \dfrac{\partial q_{d_1}}{\partial s_{d_1}} = 0, \\ \dfrac{\partial A_{d_2}}{\partial t} + \dfrac{\partial q_{d_2}}{\partial s_{d_2}} = 0, \end{cases} \tag{2.35}$$

where the subscripts M, d_1 and d_2 denote the mother and two daughter vessels, respectively. These conditions are identical for different shapes of bifurcation boundary, as shown in figure 2.

The multiscale coupling between the vascular tree and capillary–tissue system is imposed at source points $\boldsymbol{x} = \boldsymbol{x}_n$ with $n = 1, \ldots, N_{cap}$. In this work, source points are uniformly distributed to ensure full perfusion of the tissue. These points correspond to the positions where structured trees connect the superficial vessels to capillary bed, and the flow within each structured tree is described by the Poiseuille equation (2.14). Specifically, the pressure–flow relations for structured trees connected to superficial arterioles and venules are given by

$$p_{out,arteriole} - p_{cap}(\boldsymbol{x}_n) = R_{a,eq}(\boldsymbol{x}_n) q_n, \tag{2.36}$$

$$p_{cap}(\boldsymbol{x}_i) - p_{in,venule} = -R_{v,eq}(\boldsymbol{x}_i) q_i, \tag{2.37}$$

respectively, where $R_{a,eq}(\boldsymbol{x}_n)$ and $R_{v,eq}(\boldsymbol{x}_i)$ are the equivalent resistances of structured trees at $\boldsymbol{x}_n$ and $\boldsymbol{x}_i$, respectively, computed using (2.16), (2.17) and (2.15). The variables $p_{out,arteriole}$ and $p_{in,venule}$ are outlet and inlet pressures of the terminal vessel in the vascular tree, respectively, and q_n is the flow rate at terminal arteriole outlet (or venule inlet). The coupling conditions (2.36) and (2.37) are imposed using the analytic solution for p_{cap}, which is derived in the following section.

2.4. *Summary of multiscale model*

Arterioles and venules in the superficial layer of the retina are constructed using an L-system, and the flow in them is described by the 1-D model (2.1). Smaller vessels in the deep layer are generated using a structured tree model and treated as effective resistors, providing resistive boundary conditions for the 1-D model. The superficial arterioles and venules are coupled to capillaries through discrete point sources, with

https://doi.org/10.1017/jfm.2026.11820 Published online by Cambridge University Press

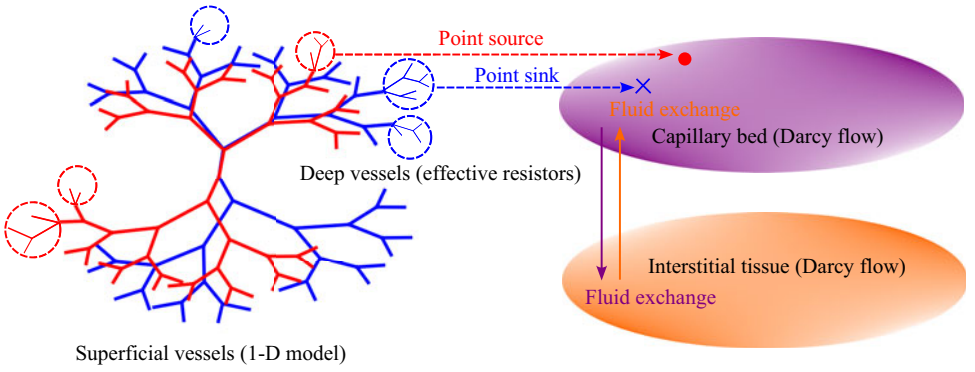


Figure 3. Schematic of the multiscale model. The arteriolar and venular trees in the superficial layer and those in the deep layer (vessels within dashed circles) are shown on the left, while the capillary bed and interstitial tissue are depicted on the right. The flow in superficial vessels is described by the 1-D model, whereas the flow in the capillary bed and interstitial tissue is modelled as the Darcy flow. The vessels in deep layer are modelled as effective resistors to set the resistive boundary condition for the arteriolar/venular trees in the superficial layer. The vasculature is coupled through the point sources (red circle) and sinks (blue cross) located in capillary bed, and capillary continuum and interstitial tissue are coupled through fluid exchange, denoted by orange and purple arrows.

the coupling imposed via the pressure–flow relations (2.36) and (2.37). The capillary bed and surrounding tissue are modelled as interacting porous media, described by two coupled continuum Darcy models (2.26). This multiscale model enables a comprehensive description of retinal haemodynamics, from large feeding vessels to the capillary level, including the fluid exchange between the vasculature and the interstitial tissue. A schematic of the multiscale model is shown in figure 3.

3. Analytic solution for capillary–tissue coupled system

3.1. *Solutions for capillary and tissue pressures*

We denote the capillary and tissue conductivities as $\kappa_{cap} = k_{cap}/\mu_{cap}$ and $\kappa_t = k_t/\mu_t$, respectively. With the transformed capillary pressure $\tilde{p}_{cap} = p_{cap} - \alpha_r \Delta\pi$, the coupled system can be expressed as

$$\begin{cases} -\kappa_{cap}\nabla^2 \tilde{p}_{cap} = \displaystyle\sum_{n=1}^{N_{cap}} q_n \delta(\boldsymbol{x} - \boldsymbol{x}_n) - \alpha_{exch}(\tilde{p}_{cap} - p_t) \quad \text{in} \quad \Omega_t, \\ -\kappa_t \nabla^2 p_t = \alpha_{exch}(\tilde{p}_{cap} - p_t) \quad \text{in} \quad \Omega_t, \end{cases} \tag{3.1}$$

which is subject to the following boundary conditions:

$$\begin{cases} -\kappa_{cap}\nabla \tilde{p}_{cap} \cdot \boldsymbol{n} = 0 \quad \text{on} \quad \partial\Omega_t, \\ -\kappa_t \nabla p_t \cdot \boldsymbol{n} = 0 \quad \text{on} \quad \partial\Omega_t. \end{cases} \tag{3.2}$$

To solve the capillary–tissue coupled system, we begin by writing the equations in matrix form

$$-\nabla^2 \begin{bmatrix} \tilde{p}_{cap} \\ p_t \end{bmatrix} = \boldsymbol{C} \begin{bmatrix} \tilde{p}_{cap} \\ p_t \end{bmatrix} + \begin{bmatrix} \dfrac{1}{\kappa_{cap}} \sum_n q_n \delta(\boldsymbol{x} - \boldsymbol{x}_n) \\ 0 \end{bmatrix}, \tag{3.3}$$

https://doi.org/10.1017/jfm.2026.11820 Published online by Cambridge University Press

where the matrix $\boldsymbol{C}$ is given by

$$\boldsymbol{C} = \alpha_{exch} \begin{bmatrix} -1/\kappa_{cap} & 1/\kappa_{cap} \\ 1/\kappa_t & -1/\kappa_t \end{bmatrix}. \tag{3.4}$$

The system is decoupled via the following transformation to new variables:

$$\begin{bmatrix} p_{mean} \\ p_{exch} \end{bmatrix} = \boldsymbol{T} \begin{bmatrix} \tilde{p}_{cap} \\ p_t \end{bmatrix}, \tag{3.5}$$

where p_{mean} is the conductivity weighted average pressure, p_{exch} is the exchange pressure proportional to their difference and $\boldsymbol{T}$ is the transformation matrix given by

$$\boldsymbol{T} = \frac{\kappa_{cap}}{\kappa_{cap} + \kappa_t} \begin{bmatrix} 1 & \kappa_t/\kappa_{cap} \\ -1 & 1 \end{bmatrix}. \tag{3.6}$$

Using this transformation, the boundary conditions become

$$\begin{cases} -\kappa_{cap} \nabla p_{mean} \cdot \boldsymbol{n} = 0 \quad \text{on} \quad \partial\Omega_t, \\ -\kappa_t \nabla p_{exch} \cdot \boldsymbol{n} = 0 \quad \text{on} \quad \partial\Omega_t. \end{cases} \tag{3.7}$$

The resulting decoupled system is then given by

$$\begin{cases} -\nabla^2 p_{mean} = \dfrac{1}{\kappa_{cap} + \kappa_t} \displaystyle\sum_{n=1}^{N_{cap}} q_n \delta(\boldsymbol{x} - \boldsymbol{x}_n) \quad \text{in} \quad \Omega_t, \\ -\nabla^2 p_{exch} + \lambda^2 p_{exch} = -\dfrac{1}{\kappa_{cap} + \kappa_t} \displaystyle\sum_{n=1}^{N_{cap}} q_n \delta(\boldsymbol{x} - \boldsymbol{x}_n) \quad \text{in} \quad \Omega_t, \end{cases} \tag{3.8}$$

where $\lambda = \sqrt{\alpha_{exch}(1/\kappa_{cap} + 1/\kappa_t)}$ and the system is subject to the boundary conditions

$$\begin{cases} \nabla p_{mean} \cdot \boldsymbol{n} = 0 \quad \text{on} \quad \partial\Omega_t, \\ \nabla p_{exch} \cdot \boldsymbol{n} = 0 \quad \text{on} \quad \partial\Omega_t. \end{cases} \tag{3.9}$$

Once the decoupled system is solved, the transformed capillary pressure and tissue pressure can be obtained through the inverse transformation that

$$\begin{bmatrix} \tilde{p}_{cap} \\ p_t \end{bmatrix} = \boldsymbol{T}^{-1} \begin{bmatrix} p_{mean} \\ p_{exch} \end{bmatrix} = \begin{bmatrix} p_{mean} - (\kappa_t/\kappa_{cap}) p_{exch} \\ p_{mean} + p_{exch} \end{bmatrix}, \tag{3.10}$$

where $\boldsymbol{T}^{-1}$ is the inverse transformation matrix given by

$$\boldsymbol{T}^{-1} = \begin{bmatrix} 1 & -\kappa_t/\kappa_{cap} \\ 1 & 1 \end{bmatrix}. \tag{3.11}$$

The capillary pressure could be obtained by adding the osmotic pressure difference to the transformed capillary pressure

$$p_{cap} = \tilde{p}_{cap} + \alpha_r \Delta\pi. \tag{3.12}$$

To solve the decoupled system, we construct the relevant Green's functions. The Green's function $f_{mean}(\boldsymbol{x}, \boldsymbol{x}')$ for p_{mean} satisfies (Kim & Jackson 1993; Riley *et al.* 2006)

$$\begin{cases} \nabla'^2 f_{mean}(\boldsymbol{x}, \boldsymbol{x}') = \delta(\boldsymbol{x} - \boldsymbol{x}') \quad \text{in} \quad \Omega_t, \\ \nabla' f_{mean}(\boldsymbol{x}, \boldsymbol{x}') \cdot \boldsymbol{n}' = 1/S \quad \text{on} \quad \partial\Omega_t, \end{cases} \tag{3.13}$$

https://doi.org/10.1017/jfm.2026.11820 Published online by Cambridge University Press

where $S = 2\pi R_t$ is the length of the boundary $\partial\Omega_t$. For this Green's function, an image point source is added at $\boldsymbol{x}'' \in \mathbb{R}^2 \setminus \Omega_t$, where $\boldsymbol{x}'' = (R_t^2/|\boldsymbol{x}|^2)\boldsymbol{x}$. The general solution for f_{mean} is then given by

$$f_{mean}(\boldsymbol{x}, \boldsymbol{x}') = \frac{1}{2\pi}\left(\log|\boldsymbol{x}' - \boldsymbol{x}| + k\log|\boldsymbol{x}' - \boldsymbol{x}''| + c\right), \tag{3.14}$$

where k and c are the constants left to be determined. The normal derivative is computed as

$$\begin{aligned}\nabla' f_{mean}(\boldsymbol{x}, \boldsymbol{x}') \cdot \boldsymbol{n}' &= \frac{1}{2\pi}\left[\frac{\boldsymbol{x}' - \boldsymbol{x}}{|\boldsymbol{x}' - \boldsymbol{x}|^2} + \frac{k(\boldsymbol{x}' - \boldsymbol{x}'')}{|\boldsymbol{x}' - \boldsymbol{x}''|^2}\right] \cdot \frac{\boldsymbol{x}'}{|\boldsymbol{x}'|} \\ &= \frac{1}{2\pi|\boldsymbol{x}'|}\left[\frac{|\boldsymbol{x}'|^2 - \boldsymbol{x}\cdot\boldsymbol{x}'}{|\boldsymbol{x}' - \boldsymbol{x}|^2} + \frac{k|\boldsymbol{x}'|^2 - k\boldsymbol{x}'\cdot\boldsymbol{x}''}{|\boldsymbol{x}' - \boldsymbol{x}''|^2}\right],\end{aligned} \tag{3.15}$$

and on the boundary $\partial\Omega_t$, where $|\boldsymbol{x}'| = R_t$, this expression simplifies to

$$\nabla' f_{mean}(\boldsymbol{x}, \boldsymbol{x}') \cdot \boldsymbol{n}' = \frac{1}{2\pi R_t}\frac{1}{|\boldsymbol{x}' - \boldsymbol{x}|^2}\left[|\boldsymbol{x}'|^2 + k|\boldsymbol{x}|^2 - (k+1)\boldsymbol{x}'\cdot\boldsymbol{x}\right]. \tag{3.16}$$

We can obtain the Green's function f_{mean} and the mean pressure by enforcing the boundary condition in problem (3.13) to solve for k. The computation of coefficients in f_{mean} and the derivation of p_{mean} are provided in Appendix A. The mean pressure p_{mean} is given by

$$p_{mean}(\boldsymbol{x}) = -\frac{1}{\kappa_{cap} + \kappa_t}\sum_{n=1}^{N_{cap}} q_n f_{mean}(\boldsymbol{x}, \boldsymbol{x}_n) + \overline{p_{mean}}, \tag{3.17}$$

where the boundary average $\overline{p_{mean}}$ is given by

$$\overline{p_{mean}} = \frac{1}{S}\int_{\partial\Omega_t} p_{mean}(\boldsymbol{x}')\mathrm{d}s'. \tag{3.18}$$

We write the variable p_{mean} in polar coordinates as

$$p_{mean}(r, \theta) = -\frac{1}{\kappa_{cap} + \kappa_t}\sum_{n=1}^{N_{cap}} q_n f_{mean}(r, \theta; r_n, \theta_n) + \overline{p_{mean}}, \tag{3.19}$$

where r_n and θ_n are radial and polar coordinates for the source point $\boldsymbol{x}_n$, respectively, and the function $f_{mean}(r, \theta; r_n, \theta_n)$ is given by

$$\begin{aligned}f_{mean}(r, \theta; r_n, \theta_n) = &\frac{1}{4\pi}\log\left(r_n^2 + r^2 - 2r_n r\cos(\theta_n - \theta)\right) \\ &+ \frac{1}{4\pi}\log\left(r_n^2 + \frac{R_t^4}{r^2} - 2r_n\frac{R_t^2}{r}\cos(\theta_n - \theta)\right).\end{aligned} \tag{3.20}$$

Figure 4 displays f_{mean} as a function of r/R_t for $r_n = 0.19R_t$ and $\theta_n = 2\pi/3$. Different colours correspond to different values of θ. All curves diverge as $r \to 0$, and when θ is close to θ_n, f_{mean} develops an increasingly sharp peak at $r = r_n$, as shown by blue, orange and red curves, which is the second logarithmic singularity. When $r \to R_t$, f_{mean} tends to finite values that depend on θ.

https://doi.org/10.1017/jfm.2026.11820 Published online by Cambridge University Press

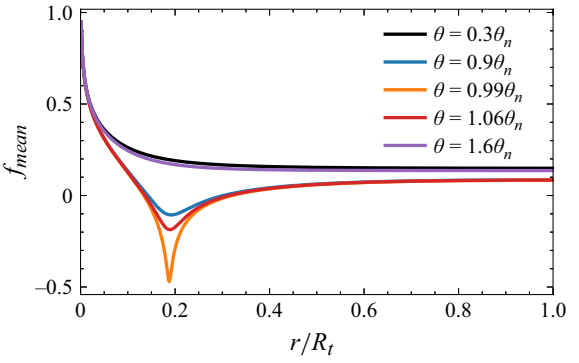


Figure 4. Behaviour of f_{mean} on r/R_t for a single source at $(r_n, \theta_n) = (0.19R_t, 2\pi/3)$. Different colours correspond to various values of θ.

When implementing the solution for p_{mean}, the conservation of mass should be enforced explicitly, which is given by

$$0 = \sum_{n=1}^{N_{cap}} q_n. \tag{3.21}$$

That is, the total flow entering capillary bed from arteriolar tree equals to the total flow drained into venules. This consistency condition could also be derived by integrating the solution for p_{mean} over the boundary

$$\overline{p_{mean}} = -\frac{1}{S}\frac{1}{\kappa_{cap}+\kappa_t}\sum_{n=1}^{N_{cap}} q_n \int_{\partial\Omega_t} f_{mean}(r, \theta; r_n, \theta_n)\mathrm{d}s + \overline{p_{mean}}, \tag{3.22}$$

which implies that

$$0 = -\frac{1}{S}\frac{1}{\kappa_{cap}+\kappa_t}\sum_{n=1}^{N_{cap}} q_n \int_{\partial\Omega_t} f_{mean}(r, \theta; r_n, \theta_n)\mathrm{d}s. \tag{3.23}$$

This demonstrates that the total flow is balanced, with each q_n weighted by its respective boundary integral. In other words, the boundary integral quantifies how any local flow source disturbs the averaged pressure. On the boundary $\partial\Omega_t$, where $r = R_t$, the function f_{mean} simplifies to

$$f_{mean}(R_t, \theta; r_n, \theta_n) = \frac{1}{2\pi}\log(R_t^2 + r_n^2 - 2R_t r_n\cos(\theta - \theta_n)). \tag{3.24}$$

The boundary integral can be computed using the identity that (Gradshteĭn & Zwillinger 2015, 4.224.9)

$$\int_0^{\pi} \log(a + b\cos\theta)\mathrm{d}\theta = \pi\log\frac{a+\sqrt{a^2-b^2}}{2}, \quad a \geq |b| > 0. \tag{3.25}$$

Interestingly, evaluation of the boundary integral shows it is independent of the source location

$$\int_{\partial\Omega_t} f_{mean}(r, \theta; r_n, \theta_n)\mathrm{d}s = 2R_t\log R_t. \tag{3.26}$$

https://doi.org/10.1017/jfm.2026.11820 Published online by Cambridge University Press

Thus (3.23) can be simplified to (3.21). The identical value of boundary integral for each source demonstrates that each connection to the larger vasculature, whether a feeding arteriole or a draining venule, contributes equally to the balance, which is consistent with the physiological situation that capillary plexus is highly interconnected.

The problem of the Green's function f_{exch} for p_{exch} is given by

$$\begin{cases} \nabla^2 f_{exch}(\boldsymbol{x}, \boldsymbol{x}_n) - \lambda^2 f_{exch}(\boldsymbol{x}, \boldsymbol{x}_n) = \delta(\boldsymbol{x} - \boldsymbol{x}_n) & \text{in} \quad \Omega_t, \\ \nabla f_{exch}(\boldsymbol{x}, \boldsymbol{x}_n) \cdot \boldsymbol{n} = 0 & \text{on} \quad \partial\Omega_t, \end{cases} \tag{3.27}$$

whose solution enables us to express p_{exch} as

$$p_{exch}(\boldsymbol{x}) = \frac{1}{\kappa_{cap} + \kappa_t} \sum_{n=1}^{N_{cap}} q_n f_{exch}(\boldsymbol{x}, \boldsymbol{x}_n). \tag{3.28}$$

In polar coordinates, the equation becomes

$$\frac{1}{r}\frac{\partial}{\partial r}\left(r\frac{\partial f_{exch}}{\partial r}\right) + \frac{1}{r^2}\frac{\partial^2 f_{exch}}{\partial \theta^2} - \lambda^2 f_{exch} = \frac{\delta(r - r_n)\delta(\theta - \theta_n)}{r}, \tag{3.29}$$

and substituting the trial solution $f_{exch}(r, \theta; r_n, \theta_n) = R(r)\Theta(\theta)$ leads to

$$\frac{r}{R(r)}\frac{\partial}{\partial r}\left(r\frac{\partial R(r)}{\partial r}\right) + \frac{1}{\Theta(\theta)}\frac{\partial^2 \Theta(\theta)}{\partial \theta^2} - \lambda^2 r^2 = 0 \tag{3.30}$$

as $(r, \theta) \neq (r_n, \theta_n)$, which yields

$$\frac{d^2\Theta}{\mathrm{d}\theta^2} + m^2\Theta = 0, \tag{3.31}$$

where periodicity in θ (with period 2π) requires that $m \in \mathbb{Z}$ and its solution is composed of $\exp(im\theta)$ and $\exp(-im\theta)$. Together with the Fourier expansion of $\delta(\theta - \theta_n)$ that

$$\delta(\theta - \theta_n) = \frac{1}{2\pi} \sum_{m=-\infty}^{\infty} \exp[im(\theta - \theta_n)], \tag{3.32}$$

we thus assume the solution is

$$f_{exch}(r, \theta; r_n, \theta_n) = \frac{1}{2\pi} \sum_{m=-\infty}^{\infty} R_{m,n}(r) \exp[im(\theta - \theta_n)], \tag{3.33}$$

which yields the following eigenvalue problem:

$$\frac{1}{r}\frac{d}{\mathrm{d}r}\left(r\frac{\mathrm{d}R_{m,n}}{\mathrm{d}r}\right) - \left(\frac{m^2}{r^2} + \lambda^2\right) R_{m,n} = \frac{\delta(r - r_n)}{r}. \tag{3.34}$$

Equation (3.34) is a modified Bessel equation and its general solution, constrained to be finite at $r = 0$, is given by

$$R_{m,n}(r) = \begin{cases} A_{m,n} I_m(\lambda r), & r \leq r_n, \\ B_{m,n} I_m(\lambda r) + C_{m,n} K_m(\lambda r), & r > r_n, \end{cases} \tag{3.35}$$

where $I_m(\lambda r)$ and $K_m(\lambda r)$ are the modified Bessel functions of order m, and $A_{m,n}$, $B_{m,n}$ as well as $C_{m,n}$ are the coefficients left to determine, and a detailed computation for them is provided in Appendix B. The radial component in (3.33) is given by

$$R_{m,n}(r) = I_m(\lambda r_<^n)\left[\frac{K_m'(\lambda R_t)}{I_m'(\lambda R_t)} I_m(\lambda r_>^n) - K_m(\lambda r_>^n)\right], \tag{3.36}$$

https://doi.org/10.1017/jfm.2026.11820 Published online by Cambridge University Press

with $r_<^n = \min(r, r_n)$ and $r_>^n = \max(r, r_n)$. Plugging the expression of f_{exch} into (3.28) with (3.36) yields

$$p_{exch}(r,\theta) = \frac{1}{2\pi(\kappa_{cap}+\kappa_t)} \sum_{n=1}^{N_{cap}} \sum_{m=-\infty}^{\infty} q_n R_{m,n}(r) \exp[im(\theta-\theta_n)]. \tag{3.37}$$

With Green's functions for mean and exchange pressures, we denote the modified Green's functions for capillary and tissue pressures as

$$G_{cap}(r,\theta;r_n,\theta_n) = f_{mean}(r,\theta;r_n,\theta_n) + \frac{\kappa_t}{\kappa_{cap}} f_{exch}(r,\theta;r_n,\theta_n), \tag{3.38}$$

$$G_t(r,\theta;r_n,\theta_n) = f_{mean}(r,\theta;r_n,\theta_n) - f_{exch}(r,\theta;r_n,\theta_n), \tag{3.39}$$

where the functions f_{mean} and f_{exch} are given by (3.20) and (3.33), respectively, and the pressures can then be expressed as

$$p_{cap}(r,\theta) = -\frac{1}{\kappa_{cap}+\kappa_t} \sum_{n=1}^{N_{cap}} q_n G_{cap}(r,\theta;r_n,\theta_n) + \overline{p_{mean}} + \alpha_r \Delta\pi, \tag{3.40}$$

$$p_t(r,\theta) = -\frac{1}{\kappa_{cap}+\kappa_t} \sum_{n=1}^{N_{cap}} q_n G_t(r,\theta;r_n,\theta_n) + \overline{p_{mean}}. \tag{3.41}$$

3.2. *Convergence of the series solution for exchange pressure*

The solution for p_{exch} is constructed by superimposing the contributions from all source points, where the kernel f_{exch} at each source is expressed as an infinite series (3.33). In order to analyse its convergence, f_{exch} is decomposed into two components as

$$f_{exch} = s_1 + s_2, \tag{3.42}$$

where

$$s_1 = \frac{1}{2\pi} \sum_{m=-\infty}^{\infty} I_m(\lambda r_<^n) \frac{K_m'(\lambda R_t)}{I_m'(\lambda R_t)} I_m(\lambda r_>^n) \exp[im(\theta-\theta_n)], \tag{3.43}$$

$$s_2 = -\frac{1}{2\pi} \sum_{m=-\infty}^{\infty} I_m(\lambda r_<^n) K_m(\lambda r_>^n) \exp[im(\theta-\theta_n)]. \tag{3.44}$$

As discussed in Appendix C, the terms in s_1 become negligible compared with those in s_2 for large m, which implies the following approximation for the radial component:

$$R_{m,n}(r) \simeq -I_m(\lambda r_<^n) K_m(\lambda r_>^n), \tag{3.45}$$

and as a result f_{exch} is effectively approximated by s_2. The radial component depends on the parameter $\lambda = \sqrt{\alpha_{exch}(1/\kappa_{cap} + 1/\kappa_t)}$, and thus its value varies with α_{exch} and $1/\kappa_{cap} + 1/\kappa_t$. The accuracy of the approximation (3.45) is explored below for varying α_{exch} and fixed permeabilities.

Figure 5 displays the dependence of radial component on the order m, where circles denote the exact values from (3.36) and lines represent the approximation (3.45). Subfigures (*a*), (*b*), (*c*) and (*d*) show the results for exchange rate of $\alpha_{exch} = 2\times10^{-5}$, $\alpha_{exch} = 2\times10^{-4}$, $\alpha_{exch} = 2\times10^{-3}$ and $\alpha_{exch} = 2\times10^{-2}\,\mu\mathrm{m\,s\,g^{-1}}$, respectively. The approximation (3.45) is nearly identical to the exact value across various values of the radial variable, even yielding a good estimate at $r = R_t$. These results demonstrate that

https://doi.org/10.1017/jfm.2026.11820 Published online by Cambridge University Press

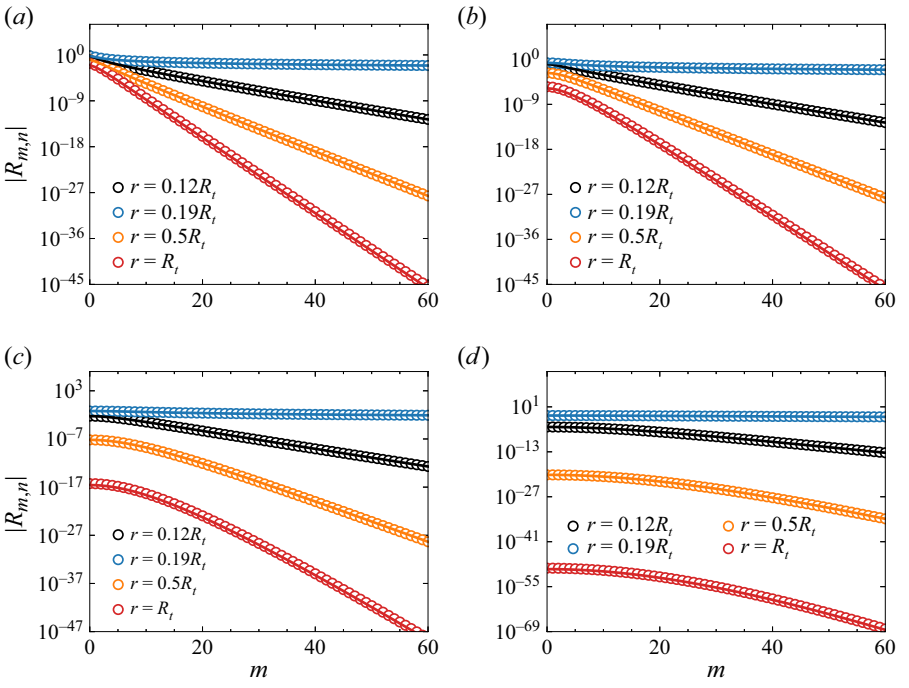


Figure 5. Dependence of radial component $R_{m,n}$ on the order m for a source located at $r_n = 0.19R_t$. Circles are the exact values of radial component computed by (3.36), while lines denote the approximation (3.45). Results are shown for four values of exchange rate: (*a*) $\alpha_{exch} = 2 \times 10^{-5}\ \mu\text{m s g}^{-1}$, (*b*) $\alpha_{exch} = 2 \times 10^{-4}\ \mu\text{m s g}^{-1}$, (*c*) $\alpha_{exch} = 2 \times 10^{-3}\ \mu\text{m s g}^{-1}$ and (*d*) $\alpha_{exch} = 2 \times 10^{-2}\ \mu\text{m s g}^{-1}$. Other parameter values are $k_{cap} = 0.03\ \mu\text{m}^2$ and $k_t = 2 \times 10^{-4}\ \mu\text{m}^2$. Different colours correspond to various values of the radial coordinate of the source.

the expression (3.45) provides an excellent estimate for the radial component despite parameter variations, and thus the convergence of f_{exch} is equivalent to that of the series s_2.

The convergence of s_2 can be established by the following relative ratio:

$$\mathcal{E}_{m,m+1} = \frac{K_{m+1}(\lambda r_>^n)}{K_m(\lambda r_>^n)} \frac{I_{m+1}(\lambda r_<^n)}{I_m(\lambda r_<^n)}. \tag{3.46}$$

Using the inequalities that (Ruiz-Antolín & Segura 2016, Theorems 2 and 7)

$$\frac{K_{m+1}(\lambda r)}{K_m(\lambda r)} < \frac{m + \frac{1}{2} + \sqrt{\left(m + \frac{1}{2}\right)^2 + (\lambda r)^2}}{\lambda r}, \quad m \geq -1/2, \tag{3.47}$$

$$\frac{I_{m+1}(\lambda r)}{I_m(\lambda r)} < \frac{\lambda r}{m + \frac{1}{2} + \sqrt{\left(m + \frac{1}{2}\right)^2 + (\lambda r)^2}}, \quad m \geq -1/2, \tag{3.48}$$

https://doi.org/10.1017/jfm.2026.11820 Published online by Cambridge University Press

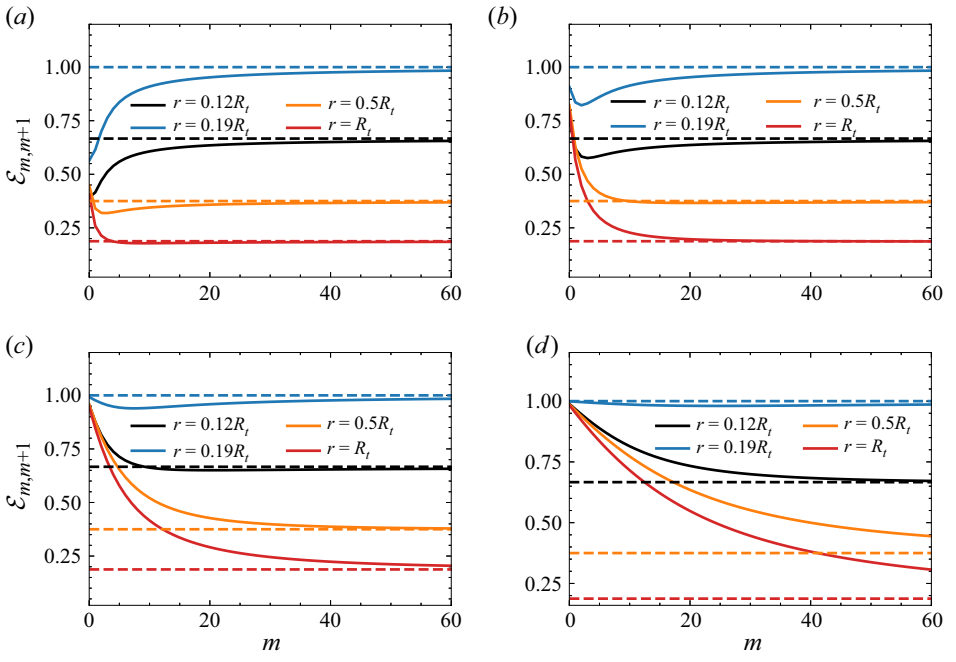


Figure 6. Dependence of relative ratio $\mathcal{E}_{m,m+1}$ on the order m for a source located at $r_n = 0.19R_t$. Solid lines denote the values of relative ratio while dashed lines are the upper bound. Results are shown for four values of exchange rate: (*a*) $\alpha_{exch} = 2 \times 10^{-5}\ \mu\text{m s g}^{-1}$, (*b*) $\alpha_{exch} = 2 \times 10^{-4}\ \mu\text{m s g}^{-1}$, (*c*) $\alpha_{exch} = 2 \times 10^{-3}\ \mu\text{m s g}^{-1}$ and (*d*) $\alpha_{exch} = 2 \times 10^{-2}\ \mu\text{m s g}^{-1}$. Other parameter values are $k_{cap} = 0.03\ \mu\text{m}^2$ and $k_t = 2 \times 10^{-4}\ \mu\text{m}^2$. Different colours correspond to various values of the radial coordinate of the source.

we obtain

$$\mathcal{E}_{m,m+1} < \frac{m + \frac{1}{2} + \sqrt{\left(m + \frac{1}{2}\right)^2 + (\lambda r_>^n)^2}}{m + \frac{1}{2} + \sqrt{\left(m + \frac{1}{2}\right)^2 + (\lambda r_<^n)^2}} \frac{r_<^n}{r_>^n}, \tag{3.49}$$

thus for all r and sufficiently large m, the ratio satisfies

$$\mathcal{E}_{m,m+1} < \frac{\min\{r, r_n\}}{\max\{r, r_n\}} \leq 1. \tag{3.50}$$

Figure 6 illustrates the dependence of relative ratio on the order m, where solid lines represent the values of relative ratio and dashed lines are the upper bound $\min\{r, r_n\}/\max\{r, r_n\}$, and different colours correspond to various values of radial coordinate. Subfigures (*a*) and (*b*) show the results for exchange rates of $\alpha_{exch} = 2 \times 10^{-5}$ and $\alpha_{exch} = 2 \times 10^{-4}\ \mu\text{m s g}^{-1}$, respectively. When m increases, the relative ratio approaches the upper bound and remains strictly below it for large m. Subfigure (*c*) shows the result for an exchange rate of $\alpha_{exch} = 2 \times 10^{-3}\ \mu\text{m s g}^{-1}$, and the relative ratio converges to upper bound and remains strictly below it, except at $r = 0.5R_t$ and $r = R_t$. As the exchange rate becomes larger, as shown in figure 6(*d*), the convergence of relative ratio toward the bound is slower, but the ratio is still less than 1.

https://doi.org/10.1017/jfm.2026.11820 Published online by Cambridge University Press

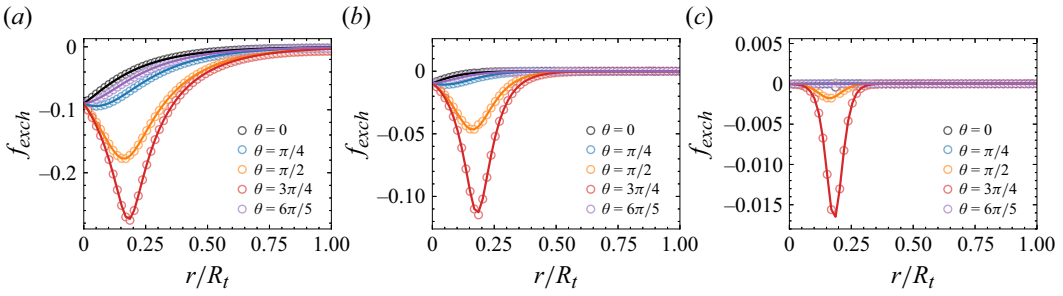


Figure 7. Behaviour of f_{exch} on r/R_t with $r_n = 0.19R_t$ and $\theta_n = 2\pi/3$. Circles are results of the truncation (3.33) with order $M = 26$, while lines are the values of approximation (3.55). Different colours correspond to various values of θ. Results are shown for three values of exchange rate: (*a*) $\alpha_{exch} = 2 \times 10^{-5}$ μm s g^{-1}, (*b*) $\alpha_{exch} = 2 \times 10^{-4}$ μm s g^{-1}, (*c*) $\alpha_{exch} = 2 \times 10^{-3}$ μm s g^{-1}. Other parameter values are $k_{cap} = 0.03$ μm^2 and $k_t = 2 \times 10^{-4}$ μm^2.

Since s_2 can be expressed as

$$s_2 = -\frac{1}{2\pi} I_0(\lambda r_<^n) K_0(\lambda r_>^n) - \frac{1}{\pi} \sum_{m=1}^{\infty} I_m(\lambda r_<^n) K_m(\lambda r_>^n) \cos[m(\theta - \theta_n)], \tag{3.51}$$

using (3.50) we obtain the following inequality:

$$|s_2| \le \frac{1}{\pi} I_0(\lambda r_<^n) K_0(\lambda r_>^n) \left(\frac{1}{2} + \sum_{m=1}^{\infty} \left(\frac{\min\{r, r_n\}}{\max\{r, r_n\}} \right)^m \right), \tag{3.52}$$

and evaluating the series yields

$$|s_2| \le \frac{1}{\pi} I_0(\lambda r_<^n) K_0(\lambda r_>^n) \frac{1 + \min\{r, r_n\}/\max\{r, r_n\}}{2\,(1 - \min\{r, r_n\}/\max\{r, r_n\})}, \tag{3.53}$$

which implies the convergence of s_2. Thus, f_{exch} converges asymptotically, with the same rate as s_2. The series s_2 can be written in a more compact expression using the following addition formula for modified Bessel functions:

$$K_0(\lambda \xi_n) = \sum_{m=-\infty}^{\infty} I_m(\lambda r_<^n) K_m(\lambda r_>^n) \exp[im(\theta - \theta_n)], \tag{3.54}$$

where $\xi_n = \sqrt{r^2 + r_n^2 - 2rr_n \cos(\theta - \theta_n)}$ is the distance between field point and source point. This identity can be considered as the counterpart of Graf addition formula for Bessel functions (Abramowitz & Stegun 2013), and is briefly proved in Appendix D. The addition formula for modified Bessel functions implies that

$$f_{exch}(r, \theta; r_n, \theta_n) \simeq -\frac{1}{2\pi} K_0(\lambda \xi_n). \tag{3.55}$$

Using the addition formula f_{exch} can be written as

$$f_{exch} = -\frac{1}{2\pi} K_0(\lambda \xi_n) + \frac{1}{2\pi} \sum_{m=-\infty}^{\infty} I_m(\lambda r_<^n) \frac{K_m'(\lambda R_t)}{I_m'(\lambda R_t)} I_m(\lambda r_>^n) \exp[im(\theta - \theta_n)]. \tag{3.56}$$

Figure 7 illustrates the behaviour of f_{exch} across r/R_t for various values of parameters, where circles denote the truncation of f_{exch} with truncation order $M = 26$ and lines represent the free-space approximation (3.55). For three values of exchange rate, the

https://doi.org/10.1017/jfm.2026.11820 Published online by Cambridge University Press

free-space approximation agrees closely with the truncation across most of the domain. However, for the curves with θ close to θ_n, such as the purple curve, the approximation deviates from the truncation.

These results, on the one hand, demonstrate the asymptotic convergence of f_{exch}. On the other hand, they also suggest how to model tissue with a complicated, irregular shape. The capillary–tissue coupled system can be decoupled into mean pressure p_{mean} and exchange pressure p_{exch}. The mean pressure, which might be sensitive to the boundary, can be solved numerically, while the exchange pressure, which governs perfusion, can be effectively approximated using the free-space solution (3.55).

3.3. *Domain-averaged pressures*

In addition to the spatial pressure fields, we compute the domain average of capillary and tissue pressures. These global metrics could provide a compact summary of model behaviours and facilitate new experimental observations.

The domain-averaged pressures are given by

$$\langle p_{cap}\rangle = \frac{1}{A_t}\int_{\Omega_t} p_{cap}\mathrm{d}\boldsymbol{x} = -\frac{1}{\kappa_{cap}+\kappa_t}\sum_{n=1}^{N_{cap}} q_n\langle G_{cap}(r_n,\theta_n)\rangle + \overline{p_{mean}} + \alpha_r\Delta\pi, \tag{3.57}$$

$$\langle p_t\rangle = \frac{1}{A_t}\int_{\Omega_t} p_t\mathrm{d}\boldsymbol{x} = -\frac{1}{\kappa_{cap}+\kappa_t}\sum_{n=1}^{N_{cap}} q_n\langle G_t(r_n,\theta_n)\rangle + \overline{p_{mean}}, \tag{3.58}$$

where $A_t = \pi R_t^2$ is the area of tissue domain and

$$\langle G_{cap}(r_n,\theta_n)\rangle = \frac{1}{A_t}\int_0^{2\pi}\int_0^{R_t} G_{cap}(r,\theta;r_n,\theta_n)r\mathrm{d}r\mathrm{d}\theta, \tag{3.59}$$

$$\langle G_t(r_n,\theta_n)\rangle = \frac{1}{A_t}\int_0^{2\pi}\int_0^{R_t} G_t(r,\theta;r_n,\theta_n)r\mathrm{d}r\mathrm{d}\theta, \tag{3.60}$$

which vary with source point (r_n,θ_n). The domain averages $\langle G_{cap}(r_n,\theta_n)$ and $\langle G_t(r_n,\theta_n)$ can be expressed as

$$\langle G_{cap}(r_n,\theta_n)\rangle = \langle f_{mean}(r_n,\theta_n)\rangle + \frac{\kappa_t}{\kappa_{cap}}\langle f_{exch}(r_n,\theta_n)\rangle, \tag{3.61}$$

$$\langle G_t(r_n,\theta_n)\rangle = \langle f_{mean}(r_n,\theta_n)\rangle - \langle f_{exch}(r_n,\theta_n)\rangle, \tag{3.62}$$

where domain averages $\langle f_{mean}(r_n,\theta_n)\rangle$ and $\langle f_{exch}(r_n,\theta_n)\rangle$ vary with (r_n,θ_n) as well. From the problem (3.27) the domain average $\langle f_{exch}(r_n,\theta_n)\rangle$ is computed as follows:

$$\begin{aligned}\langle f_{exch}(r_n,\theta_n)\rangle &= \frac{1}{\lambda^2 A_t}\int_{\Omega_t}\nabla^2 f_{exch}\mathrm{d}\boldsymbol{x} - \frac{1}{\lambda^2 A_t}\\ &= \frac{1}{\lambda^2 A_t}\int_{\partial\Omega_t}\nabla f_{exch}\cdot\boldsymbol{n}\mathrm{d}s - \frac{1}{\lambda^2 A_t}\\ &= -\frac{1}{\lambda^2 A_t}.\end{aligned} \tag{3.63}$$

https://doi.org/10.1017/jfm.2026.11820 Published online by Cambridge University Press

The domain average $\langle f_{mean}(r_n, \theta_n)\rangle$ is given by

$$\langle f_{mean}(r_n, \theta_n)\rangle = a_1 + a_2, \tag{3.64}$$

where

$$a_1 = \frac{1}{4\pi A_t}\int_0^{2\pi}\int_0^{R_t} \log\left(r_n^2 + r^2 - 2r_n r\cos(\theta_n - \theta)\right) r\,\mathrm{d}r\,\mathrm{d}\theta, \tag{3.65}$$

$$a_2 = \frac{1}{4\pi A_t}\int_0^{2\pi}\int_0^{R_t} \log\left(r_n^2 + \frac{R_t^4}{r^2} - 2r_n\frac{R_t^2}{r}\cos(\theta_n - \theta)\right) r\,\mathrm{d}r\,\mathrm{d}\theta. \tag{3.66}$$

Evaluating a_1 and a_2 using the (3.25) yields

$$a_1 = \frac{1}{2\pi}\log R_t - \frac{1}{4\pi} + \frac{r_n^2}{4\pi R_t^2}, \tag{3.67}$$

$$a_2 = \frac{1}{2\pi}\log R_t + \frac{1}{4\pi}. \tag{3.68}$$

Thus,

$$\langle f_{mean}(r_n, \theta_n)\rangle = \frac{1}{\pi}\log R_t + \frac{r_n^2}{4\pi R_t^2}, \tag{3.69}$$

and

$$\langle G_{cap}(r_n, \theta_n)\rangle = \frac{1}{\pi}\log R_t + \frac{r_n^2}{4\pi R_t^2} - \frac{\kappa_t}{\kappa_{cap}}\frac{1}{\lambda^2\pi R_t^2}, \tag{3.70}$$

$$\langle G_t(r_n, \theta_n)\rangle = \frac{1}{\pi}\log R_t + \frac{r_n^2}{4\pi R_t^2} + \frac{1}{\lambda^2\pi R_t^2}, \tag{3.71}$$

then the domain-averaged pressures are given by

$$\langle p_{cap}\rangle = -\frac{1}{\pi(\kappa_{cap}+\kappa_t)}\sum_{n=1}^{N_{cap}} q_n\left(\log R_t + \frac{r_n^2}{4R_t^2} - \frac{\kappa_t}{\kappa_{cap}}\frac{1}{\lambda^2 R_t^2}\right) + \overline{p_{mean}} + \alpha_r\Delta\pi, \tag{3.72}$$

$$\langle p_t\rangle = -\frac{1}{\pi(\kappa_{cap}+\kappa_t)}\sum_{n=1}^{N_{cap}} q_n\left(\log R_t + \frac{r_n^2}{4R_t^2} + \frac{1}{\lambda^2 R_t^2}\right) + \overline{p_{mean}}. \tag{3.73}$$

These expressions reveal that vessels contribute disproportionately to global retinal fluid balance.

4. Numerical methods

4.1. *Finite volume method for 1-D model*

We solve the 1-D blood flow model using the finite volume method (FVM) (Olufsen *et al.* 2000; Kolachalama *et al.* 2007). The governing equations are expressed in conservative form

$$\frac{\partial \boldsymbol{U}}{\partial t} + \frac{\partial \boldsymbol{F}}{\partial s} = \boldsymbol{S}, \tag{4.1}$$

https://doi.org/10.1017/jfm.2026.11820 Published online by Cambridge University Press

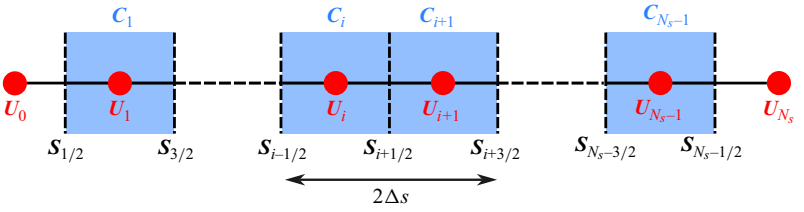


Figure 8. Spatial discretisation of the vessel.

where state, flux and source vectors are given by

$$\boldsymbol{U} = (A, q)^T, \tag{4.2}$$

$$\boldsymbol{F} = \left(q, \frac{4}{3}\frac{q^2}{A} + \frac{K}{\rho}\left(\frac{\beta_1}{\beta_1+1}\frac{A^{\beta_1+1}}{A_0^{\beta_1}} - \frac{\beta_2}{\beta_2+1}\frac{A^{\beta_2+1}}{A_0^{\beta_2}} \right) \right)^T, \tag{4.3}$$

$$\boldsymbol{S} = \left(0, C_f\right)^T, \tag{4.4}$$

respectively. The vessel domain $0 \le s \le l_v$ is discretised into $N_s + 1$ spatial points at $s_i = i\Delta s$ with $i = 0, \ldots, N_s$ and $\Delta s = l_v/N_s$. The cell centres are located at s_i with $1 \le i \le N_s - 1$, the cells are $C_i = [s_{i-1/2}, s_{i+1/2}] = [(i-1/2)\Delta s, (i+1/2)\Delta s]$ and the boundaries are at $s_0 = 0$ and $s_{N_s} = l_v$, as shown in figure 8. The time is discretised into steps $t_n = n\Delta t$ with $0 \le n \le N_t$. The FVM is implemented on C_i over $[t_n, t_{n+1}]$ while boundary conditions are enforced at s_0 and s_{N_s}.

We next describe the FVM for interior points. Integrating equation (4.1) over the control volume $C_i \times [t_n, t_{n+1}]$ yields

$$\int_{t_n}^{t_{n+1}} \int_{C_i} \boldsymbol{S}(s,t)\mathrm{d}s\mathrm{d}t = \int_{C_i} \left[\boldsymbol{U}(s,t_{n+1}) - \boldsymbol{U}(s,t_n)\right]\mathrm{d}s + \int_{t_n}^{t_{n+1}} \left[\boldsymbol{F}(s_{i+1/2},t) - \boldsymbol{F}(s_{i-1/2},t)\right]\mathrm{d}t. \tag{4.5}$$

The integrals can be approximated as

$$\int_{s_{i-1/2}}^{s_{i+1/2}} \boldsymbol{U}(s,t_{n+1})\mathrm{d}s \approx \Delta s \boldsymbol{U}_i^{n+1}, \tag{4.6}$$

$$\int_{t_n}^{t_{n+1}} \boldsymbol{F}(s_{i+1/2},t)\mathrm{d}t \approx \Delta t \boldsymbol{F}_{i+1/2}^{n+1/2}, \tag{4.7}$$

$$\int_{t_n}^{t_{n+1}} \int_{s_{i-1/2}}^{s_{i+1/2}} \boldsymbol{S}(s,t)\mathrm{d}s\mathrm{d}t \approx \frac{\Delta s \Delta t}{2}\left(\boldsymbol{S}_{i+1/2}^{n+1/2} + \boldsymbol{S}_{i-1/2}^{n+1/2}\right), \tag{4.8}$$

where $\boldsymbol{U}_i^{n+1} = \boldsymbol{U}(s_i, t_{n+1})$, and similar notations are used for flux and source vectors. Thus FVM equation becomes

$$\boldsymbol{U}_i^{n+1} = \boldsymbol{U}_i^n - \frac{\Delta t}{\Delta s}\left(\boldsymbol{F}_{i+1/2}^{n+1/2} - \boldsymbol{F}_{i-1/2}^{n+1/2}\right) + \frac{\Delta t}{2}\left(\boldsymbol{S}_{i+1/2}^{n+1/2} + \boldsymbol{S}_{i-1/2}^{n+1/2}\right). \tag{4.9}$$

The unknown interface variables $\boldsymbol{F}_{i+1/2}^{n+1/2}$, $\boldsymbol{F}_{i-1/2}^{n+1/2}$, $\boldsymbol{S}_{i+1/2}^{n+1/2}$ and $\boldsymbol{S}_{i-1/2}^{n+1/2}$ depend on $\boldsymbol{U}_m^{n+1/2}$ with $m = i \pm 1/2$, which can be determined by the Lax–Wendroff scheme as

https://doi.org/10.1017/jfm.2026.11820 Published online by Cambridge University Press

(Kolachalama *et al.* 2007)

$$\boldsymbol{U}_m^{n+1/2} = \frac{\boldsymbol{U}_{m+1/2}^n + \boldsymbol{U}_{m-1/2}^n}{2} + \frac{\Delta t}{2}\left(-\frac{\boldsymbol{F}_{m+1/2}^n - \boldsymbol{F}_{m-1/2}^n}{\Delta s} + \frac{\boldsymbol{S}_{m+1/2}^n + \boldsymbol{S}_{m-1/2}^n}{2}\right). \tag{4.10}$$

4.2. *Implementations for boundary and multiscale coupling conditions*

4.2.1. *Boundary conditions for vascular trees*

At the CRA inlet, the area $A_{CRA,0}^{n+1}$ is determined by solving the equation

$$p_{in,CRA}(t_{n+1}) - p_{ext} = K\left[\left(\frac{A_{CRA,0}^{n+1}}{A_0}\right)^{\beta_1} - \left(\frac{A_{CRA,0}^{n+1}}{A_0}\right)^{\beta_2}\right], \tag{4.11}$$

where $p_{in,CRA}(t_{n+1})$ is the prescribed CRA inlet pressure at time t_{n+1}. The corresponding flow rate is computed by discretising the mass-conservation equation (He *et al.* 2004)

$$\frac{(A_{CRA,0}^{n+1} + A_{CRA,1}^{n+1}) - (A_{CRA,0}^{n} + A_{CRA,1}^{n})}{2\Delta t} + \frac{q_{CRA,1}^{n+1} - q_{CRA,0}^{n+1}}{\Delta s_{CRA}} = 0, \tag{4.12}$$

which yields the following equation:

$$q_{CRA,0}^{n+1} = q_{CRA,1}^{n+1} + \frac{\Delta s_{CRA}}{2\Delta t}\left[(A_{CRA,0}^{n+1} + A_{CRA,1}^{n+1}) - (A_{CRA,0}^{n} + A_{CRA,1}^{n})\right]. \tag{4.13}$$

At the CRV outlet, the area $A_{CRV,0}^{n+1}$ is obtained by solving the equation

$$p_{out,CRV} - p_{ext} = K\left[\left(\frac{A_{CRV,0}^{n+1}}{A_0}\right)^{\beta_1} - \left(\frac{A_{CRV,0}^{n+1}}{A_0}\right)^{\beta_2}\right], \tag{4.14}$$

where $p_{out,CRV}$ is the CRV outlet pressure. The flow rate at CRV outlet is determined by

$$q_{CRV,0}^{n+1} = q_{CRV,1}^{n+1}. \tag{4.15}$$

For the bifurcation boundary, the mass-conservation equations are discretised, which yields the following system at $t = t_{n+1}$ (He *et al.* 2004; Köppl & Helmig 2023):

$$\boldsymbol{Y}(\boldsymbol{x}_b) = [Y_1(\boldsymbol{x}_b), Y_2(\boldsymbol{x}_b), \ldots, Y_6(\boldsymbol{x}_b)] = \boldsymbol{0}, \tag{4.16}$$

where

$$Y_1 = q_{M,N_s}^{n+1} - q_{d_1,0}^{n+1} - q_{d_2,0}^{n+1}, \tag{4.17}$$

$$Y_2 = p_{M,N_s}^{n+1}(A_{M,N_s}^{n+1}) - p_{d_1,0}^{n+1}(A_{d_1,0}^{n+1}), \tag{4.18}$$

$$Y_3 = p_{M,N_s}^{n+1}(A_{M,N_s}^{n+1}) - p_{d_2,0}^{n+1}(A_{d_2,0}^{n+1}), \tag{4.19}$$

$$Y_4 = \frac{(A_{M,N_s}^{n+1} + A_{M,N_s-1}^{n+1}) - (A_{M,N_s}^{n} + A_{M,N_s-1}^{n})}{2\Delta t} + \frac{q_{M,N_s}^{n+1} - q_{M,N_s-1}^{n+1}}{\Delta s_M}, \tag{4.20}$$

$$Y_5 = \frac{(A_{d_1,0}^{n+1} + A_{d_1,1}^{n+1}) - (A_{d_1,0}^{n} + A_{d_1,1}^{n})}{2\Delta t} + \frac{q_{d_1,1}^{n+1} - q_{d_1,0}^{n+1}}{\Delta s_{d_1}}, \tag{4.21}$$

$$Y_6 = \frac{(A_{d_2,0}^{n+1} + A_{d_2,1}^{n+1}) - (A_{d_2,0}^{n} + A_{d_2,1}^{n})}{2\Delta t} + \frac{q_{d_2,1}^{n+1} - q_{d_2,0}^{n+1}}{\Delta s_{d_2}}, \tag{4.22}$$

https://doi.org/10.1017/jfm.2026.11820 Published online by Cambridge University Press

and the pressures $p^{n+1}_{M,N_s}(A^{n+1}_{M,N_s})$, $p^{n+1}_{d_1,0}(A^{n+1}_{d_1,0})$ and $p^{n+1}_{d_2,0}(A^{n+1}_{d_2,0})$ depend on the corresponding areas through the elastic model. The unknown variables are

$$\boldsymbol{x}_b = \left[A^{n+1}_{M,N_s}, q^{n+1}_{M,N_s}, A^{n+1}_{d_1,0}, q^{n+1}_{d_1,0}, A^{n+1}_{d_2,0}, q^{n+1}_{d_2,0}\right]^T, \tag{4.23}$$

while the interior variables of each vessel, such as A^{n+1}_{M,N_s-1} and q^{n+1}_{M,N_s-1}, are obtained by integration along each vessel. This system is solved at each time step to determine the bifurcation boundary variables.

4.2.2. *Multiscale coupling condition*

We denote the vectors of pressure and flow rate of source points at $t = t_{n+1}$ as

$$\boldsymbol{p}^{n+1}_{cap} = [p^{n+1}_{cap}(\boldsymbol{x}_1), \ldots, p^{n+1}_{cap}(\boldsymbol{x}_{N_{cap}})]^T, \tag{4.24}$$

$$\boldsymbol{q}^{n+1} = [q^{n+1}(\boldsymbol{x}_1), \ldots, q^{n+1}(\boldsymbol{x}_{N_{cap}})]^T, \tag{4.25}$$

respectively, where $p^{n+1}_{cap}(\boldsymbol{x}_i)$ and $q^{n+1}(\boldsymbol{x}_i)$ are the pressure and the flow rate at $\boldsymbol{x} = \boldsymbol{x}_i$, respectively, and N_{cap} is the number of superficial vessels connected to structured trees. We assume the Poiseuille flow in structured trees, and thus $q^{n+1}(\boldsymbol{x}_i)$ is also the flow rate in the terminal superficial vessels, which is connected to capillaries at $\boldsymbol{x} = \boldsymbol{x}_i$. We introduce the matrix $\boldsymbol{R}$, which is composed of the equivalent resistances of structured trees, given by

$$\boldsymbol{R} = \begin{bmatrix} R_{a,eq}(\boldsymbol{x}_1) & & & & & & \\ & \ddots & & & & & \\ & & R_{a,eq}(\boldsymbol{x}_i) & & & & \\ & & & R_{v,eq}(\boldsymbol{x}_{i+1}) & & & \\ & & & & \ddots & & \\ & & & & & R_{v,eq}(\boldsymbol{x}_{N_{cap}}) \end{bmatrix}, \tag{4.26}$$

where $R_{a,eq}(\boldsymbol{x}_i)$ denotes the equivalent resistance of a structured tree that connects the arteriolar tree to the capillary continuum at $\boldsymbol{x} = \boldsymbol{x}_i$ and $R_{v,eq}(\boldsymbol{x}_k)$ denotes that of a structured tree that connects the venular tree to the capillary continuum at $\boldsymbol{x} = \boldsymbol{x}_k$. The capillary pressures at source points are given by

$$\boldsymbol{p}^{n+1}_{cap} = \boldsymbol{M}^{cap}\boldsymbol{q}^{n+1} + (\overline{p_{mean}} + \alpha_r \Delta\pi)\boldsymbol{1}, \tag{4.27}$$

where $\boldsymbol{M}^{cap}$ is a resistance matrix with element $M^{cap}_{iw} = -G_{cap}(r_i, \theta_i; r_w, \theta_w)/(\kappa_{cap} + \kappa_t)$, while the Poiseuille equation for structured trees yields the following equation:

$$\boldsymbol{p}^{n+1}_{cap} = \boldsymbol{p}^{n+1} - \boldsymbol{R}\boldsymbol{q}^{n+1}, \tag{4.28}$$

where the pressure vector of the terminal vessels in superficial vascular trees $\boldsymbol{p}^{n+1}$ is given by

$$\boldsymbol{p}^{n+1} = [p^{n+1}_{1,N_s}, \ldots, p^{n+1}_{N_{cap},N_s}]^T. \tag{4.29}$$

https://doi.org/10.1017/jfm.2026.11820 Published online by Cambridge University Press

Thus the coupling condition is given by

$$\begin{cases} \boldsymbol{p}_{cap}^{n+1} = \boldsymbol{M}^{cap}\boldsymbol{q}^{n+1} + (\overline{p_{mean}} + \alpha_r \Delta\pi)\mathbf{1}, \\ \boldsymbol{p}_{cap}^{n+1} = \boldsymbol{p}^{n+1} - \boldsymbol{R}\boldsymbol{q}^{n+1}, \\ \overline{p_{mean}} = \dfrac{1}{S}\displaystyle\int_{\partial\Omega_t} p_{mean}\mathrm{d}s, \\ p_{mean}(r,\theta) = -\dfrac{1}{\kappa_{cap}+\kappa_t}\displaystyle\sum_{i=1}^{N_{cap}} q_i\, f_{mean}(r,\theta;r_i,\theta_i) + \overline{p_{mean}}, \\ \displaystyle\sum_{n=1}^{N_{cap}} q_n = 0, \end{cases} \tag{4.30}$$

where the pressures $\boldsymbol{p}^{n+1}$ are governed by the following equations in terminal vessels:

$$\begin{cases} \dfrac{\partial A_k}{\partial t} + \dfrac{\partial q_k}{\partial s} = 0, \quad k = 1, \ldots, N_{cap}, \\ p_k - p_{ext} = K\left[\left(\dfrac{A}{A_0}\right)^{\beta_1} - \left(\dfrac{A}{A_0}\right)^{\beta_2}\right], \quad k = 1, \ldots, N_{cap}, \end{cases} \tag{4.31}$$

and A_k and q_k denote the area and flow rate of the terminal vessels in superficial vascular trees, respectively.

Solving the system (4.30) directly is challenging due to the integral term, the conservation of mass and the nonlinear dependence of pressure on area. To simplify it, we begin by combining the first two equations in system (4.30), which yields the following pressure–flow relationship:

$$\boldsymbol{p}^{n+1} = \boldsymbol{R}^{cap}\boldsymbol{q}^{n+1} + (\overline{p_{mean}} + \alpha_r \Delta\pi)\mathbf{1}, \tag{4.32}$$

where $\boldsymbol{R}^{cap} = \boldsymbol{M}^{cap} + \boldsymbol{R}$. Solving for the flow rate vector yields

$$\boldsymbol{q}^{n+1} = (\boldsymbol{R}^{cap})^{-1}\boldsymbol{p}^{n+1} - (\overline{p_{mean}} + \alpha_r \Delta\pi)(\boldsymbol{R}^{cap})^{-1}\mathbf{1}, \tag{4.33}$$

and then imposing the conservation of mass leads to

$$0 = \mathbf{1}^T(\boldsymbol{R}^{cap})^{-1}\boldsymbol{p}^{n+1} - (\overline{p_{mean}} + \alpha_r \Delta\pi)\mathbf{1}^T(\boldsymbol{R}^{cap})^{-1}\mathbf{1}, \tag{4.34}$$

which implies that

$$\overline{p_{mean}} = \frac{1}{s_{cap}}\mathbf{1}^T(\boldsymbol{R}^{cap})^{-1}\boldsymbol{p}^{n+1} - \alpha_r \Delta\pi, \tag{4.35}$$

with $s_{cap} = \mathbf{1}^T(\boldsymbol{R}^{cap})^{-1}\mathbf{1}$. Substituting the expression of $\overline{p_{mean}}$ into the (4.32), we obtain

$$\boldsymbol{p}^{n+1} = \boldsymbol{R}^{cap}\boldsymbol{q}^{n+1} + \frac{1}{s_{cap}}\left[\mathbf{1}^T(\boldsymbol{R}^{cap})^{-1}\boldsymbol{p}^{n+1}\right]\mathbf{1}, \tag{4.36}$$

which consists of two unknown vectors $\boldsymbol{p}^{n+1}$ and $\boldsymbol{q}^{n+1}$. The mass-conservation equation is discretised as that for the CRA inlet and bifurcation boundary such that, for each arteriole or venule,

$$q_{k,N_s}^{n+1} = q_{k,N_s-1}^{n+1} - \frac{\Delta s_k}{2\Delta t}\left[\left(A_{k,N_s-1}^{n+1} + A_{k,N_s}^{n+1}\right) - \left(A_{k,N_s}^{n} + A_{k,N_s-1}^{n}\right)\right], \tag{4.37}$$

https://doi.org/10.1017/jfm.2026.11820 Published online by Cambridge University Press

where $k = 1, \ldots, N_{cap}$. Given that flows in structured trees are assumed to be Poiseuille flow, the flow rates are equal to those at boundaries of terminal vessels in superficial vascular trees, that is $q^{n+1}(\boldsymbol{x}_k) = q^{n+1}_{k,N_s}$. This enables us to express $\boldsymbol{q}^{n+1}$ as

$$\boldsymbol{q}^{n+1} = -\boldsymbol{B}\left[\left(\boldsymbol{A}^{n+1}_{N_s} + \boldsymbol{A}^{n+1}_{N_s-1}\right) - \left(\boldsymbol{A}^{n}_{N_s} + \boldsymbol{A}^{n}_{N_s-1}\right)\right] + \boldsymbol{f}^{n+1}, \tag{4.38}$$

where area vectors are given by

$$\boldsymbol{A}^{n+1}_{N_s} = \left[A^{n+1}_{1,N_s}, \ldots, A^{n+1}_{N_{cap},N_s}\right]^T, \tag{4.39}$$

$$\boldsymbol{A}^{n+1}_{N_s-1} = \left[A^{n+1}_{1,N_s-1}, \ldots, A^{n+1}_{N_{cap},N_s-1}\right]^T, \tag{4.40}$$

$$\boldsymbol{A}^{n}_{N_s} = \left[A^{n}_{1,N_s}, \ldots, A^{n}_{N_{cap},N_s}\right]^T, \tag{4.41}$$

$$\boldsymbol{A}^{n}_{N_s-1} = \left[A^{n}_{1,N_s-1}, \ldots, A^{n}_{N_{cap},N_s-1}\right]^T, \tag{4.42}$$

the matrix $\boldsymbol{B}$ is given by

$$\boldsymbol{B} = \begin{bmatrix} \Delta s_1/(2\Delta t) & & \\ & \ddots & \\ & & \Delta s_{N_{cap}}/(2\Delta t) \end{bmatrix}, \tag{4.43}$$

and $\boldsymbol{f}^{n+1}$ is given by

$$\boldsymbol{f}^{n+1} = \left[q^{n+1}_{1,N_s-1}, \ldots, q^{n+1}_{N_{cap},N_s-1}\right]^T. \tag{4.44}$$

The numerical implementation for the coupling condition is thus given by

$$\begin{cases} \boldsymbol{p}^{n+1} = \boldsymbol{R}^{cap}\boldsymbol{q}^{n+1} + \dfrac{1}{s_{cap}}\mathbf{1}^T(\boldsymbol{R}^{cap})^{-1}\boldsymbol{p}^{n+1}\mathbf{1}, \\ \boldsymbol{q}^{n+1} = -\boldsymbol{B}\left[\left(\boldsymbol{A}^{n+1}_{N_s} + \boldsymbol{A}^{n+1}_{N_s-1}\right) - \left(\boldsymbol{A}^{n}_{N_s} + \boldsymbol{A}^{n}_{N_s-1}\right)\right] + \boldsymbol{f}^{n+1}, \\ p^{n+1}_{k,N_s} - p_{ext} = K\left[\left(\dfrac{A^{n+1}_{k,N_s}}{A_0}\right)^{\beta_1} - \left(\dfrac{A^{n+1}_{k,N_s}}{A_0}\right)^{\beta_2}\right], \quad k = 1, \ldots, N_{cap}. \end{cases} \tag{4.45}$$

It is interesting to note that the effect of $\alpha_r \Delta\pi$ is absorbed into the domain-average $\overline{p_{mean}}$ via the conservation of mass, and the flow rates at source points are thus independent of $\alpha_r \Delta\pi$. In other words, a constant oncotic offset does not alter the pressure difference established by the fixed arteriolar and venular boundary conditions.

4.2.3. *Numerical treatments of infinite summation and the singularity*

Two main difficulties arise when implementing the Green's function for mean and exchange pressures: the infinite summation for exchange pressure, and the singularity when the field point is a source point. In what follows we show how to address these issues.

The finite-order truncation of s_1 in f_{exch} is utilised in computations. The truncation of s_1 with order M is given by

$$s_1 \approx \frac{1}{2\pi}\sum_{m=-M}^{M} I_m(\lambda r^n_<)\frac{K'_m(\lambda R_t)}{I'_m(\lambda R_t)} I_m(\lambda r^n_>)\exp[im(\theta - \theta_n)], \tag{4.46}$$

https://doi.org/10.1017/jfm.2026.11820 Published online by Cambridge University Press

since the radial component is symmetric in m, the truncation can be written as

$$s_1 \approx \frac{1}{2\pi} I_0(\lambda r_<^n) \frac{K_0'(\lambda R_t)}{I_0'(\lambda R_t)} I_0(\lambda r_>^n) + \frac{1}{\pi} \sum_{m=1}^{M} I_m(\lambda r_<^n) \frac{K_m'(\lambda R_t)}{I_m'(\lambda R_t)} I_m(\lambda r_>^n) \cos[m(\theta - \theta_n)]. \tag{4.47}$$

The truncation could be accurate with only a few terms since the high-order contributions to s_1 are negligible relative to s_2, as discussed in Appendix C.

The singularity occurs at $r = r_n$ in both $f_{mean}(r, \theta; r_n, \theta_n)$ and $f_{exch}(r, \theta; r_n, \theta_n)$, which could be solved via local domain averaging. The following averages are employed for the logarithm function and modified Bessel function of the second kind:

$$\langle \log \xi_n^2 \rangle = \frac{1}{A_n} \int_{\Omega_n} \log \xi_n^2 r \mathrm{d}r \mathrm{d}\theta, \tag{4.48}$$

$$\langle K_0(\lambda \xi_n) \rangle = \frac{1}{A_n} \int_{\Omega_n} K_0(\lambda \xi_n) r \mathrm{d}r \mathrm{d}\theta, \tag{4.49}$$

where $\xi_n = \sqrt{r^2 + r_n^2 - 2 r r_n \cos(\theta - \theta_n)}$, Ω_n is a circular domain of radius $r_{v,n}$ centred at source point $\boldsymbol{x}_n$ and A_n is its area. Such averaging, on the one hand, provides a numerical treatment for the singularity, and on the other hand, it is also physiologically reasonable, since the blood does not enter or exit the capillary bed at a point but through a vessel of finite radius $r_{v,n}$. Moreover, the pressure p_{cap} is an averaged variable over some capillaries, and averaging over the vessel cross-section thus ensures the consistency in the coupling across scales. The average for logarithmic function is given by

$$\langle \log \xi_n^2 \rangle = \frac{2}{\pi r_{v,n}^2} \int_0^{2\pi} \int_0^{r_{v,n}} \xi \log \xi \mathrm{d}\xi \mathrm{d}\theta = 2 \log r_{v,n} - 1. \tag{4.50}$$

The average for modified Bessel function of second kind can be written as

$$\langle K_0(\lambda \xi_n) \rangle = \frac{1}{\lambda^2 \pi r_{v,n}^2} \int_0^{2\pi} \int_0^{\lambda r_{v,n}} K_0(\xi) \xi \mathrm{d}\xi \mathrm{d}\theta, \tag{4.51}$$

and using the identity that $\mathrm{d}(\xi K_1(\xi))/\mathrm{d}\xi = -\xi K_0(\xi)$, it is given by

$$\langle K_0(\lambda \xi_n) \rangle = -\frac{2}{\lambda r_{v,n}} K_1(\lambda r_{v,n}) + \frac{2}{\lambda^2 r_{v,n}^2}. \tag{4.52}$$

For $r = r_n$, the Green's function of source point (r_n, θ_n) for mean pressure is implemented as

$$f_{mean}(r_n, \theta_n; r_n, \theta_n) = \frac{1}{4\pi} \left[2 \log r_{v,n} - 1 + \log \left(r_n^2 + \frac{R_t^4}{r_n^2} - 2 R_t^2 \right) \right], \tag{4.53}$$

while that for exchange pressure is

$$f_{exch}(r_n, \theta_n; r_n, \theta_n) = \frac{1}{\pi \lambda r_{v,n}} K_1(\lambda r_{v,n}) - \frac{1}{\pi \lambda^2 r_{v,n}^2} + \frac{1}{2\pi} I_0^2(\lambda r_n) \frac{K_0'(\lambda R_t)}{I_0'(\lambda R_t)} + \frac{1}{\pi} \sum_{m=1}^{M} I_m^2(\lambda r_n) \frac{K_m'(\lambda R_t)}{I_m'(\lambda R_t)}. \tag{4.54}$$

https://doi.org/10.1017/jfm.2026.11820 Published online by Cambridge University Press

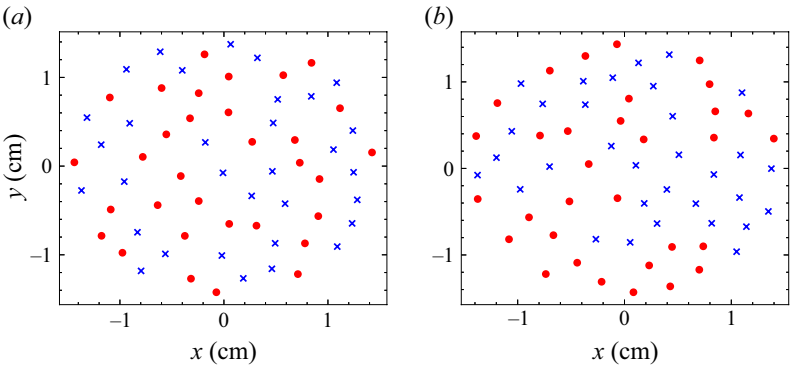


Figure 9. The distribution of randomly generated sources and sinks. The red circles and blue crosses denote the sources and sinks, respectively. (*a*) Sources and sinks in source distribution 1. (*b*) Sources and sinks in source distribution 2.

4.3. *Summary of numerical methods*

The numerical solution for the haemodynamics in retinal microcirculation at each time step is obtained as follows. First, variables at interior points of each vessel are solved using (4.9) and (4.10). Second, the boundary conditions of each vessel are determined using (4.11), (4.13), (4.14), (4.15) and (4.16). Third, the coupling condition (4.45) is solved, from which the remaining undetermined boundary variables are computed.

5. Validation of proposed multiscale model

In this section, we first establish the model's numerical robustness by exploring the dependence of total flow on the truncation order. To assess the accuracy of our model, we then validate the model's predictions against experimental data and those of established models. Third, the ability of our model to predict pulsatile pressure is shown by imposing time-dependent CRA inlet pressure. For all simulations the CRV outlet pressure is set to $p_{out,CRV} = 16$ mmHg. For steady arteriolar pressure, the CRA inlet pressure is set to a constant baseline value of $p_{in,CRA} = 62$ mmHg which is approximately the averaged pressure over one cardiac cycle (Guidoboni *et al.* 2014*b*). While values of other parameters in the 1-D model are summarised in table 1, parameters in capillary–tissue system are set to $k_{cap} = 0.03\ \mu\text{m}^2$, $k_t = 0.0002\ \mu\text{m}^2$ and $\alpha_{exch} = 2 \times 10^{-4}\ \mu\text{m s g}^{-1}$.

Two source/sink distributions are used to test whether the qualitative behaviour of the model is robust to the specific random placement of the capillary coupling points. They are generated by the following steps. First, $N_{cap} = 2 \times 2^5$ points are uniformly distributed at random over the tissue domain. These points are then matched to the 2^5 superficial arteriolar termini and 2^5 superficial venular termini as follows. The distance between every possible terminus-point pair is computed. Starting with all termini and all random points unpaired, the pair with the smallest distance is selected and the point is assigned to that terminus, which establishes the first pair. The same procedure is iterated for the remaining termini and points until every terminus is paired with a distinct random point. The random points paired to arteriolar termini are designated as sources, while those paired to venular termini are designated as sinks. The two generated source/sink distributions are shown in figure 9. In the computation for pulsatile inlet pressure only source distribution 1 is utilised.

https://doi.org/10.1017/jfm.2026.11820 Published online by Cambridge University Press

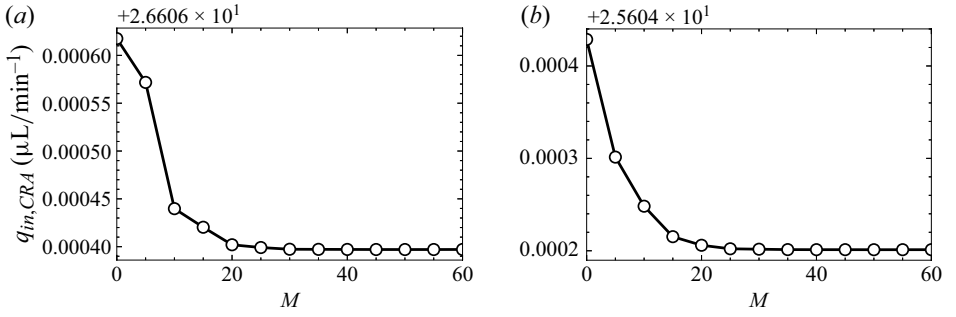


Figure 10. Dependence of total flow on truncation order M. (a) Result with source distribution 1. (b) Result with source distribution 2.

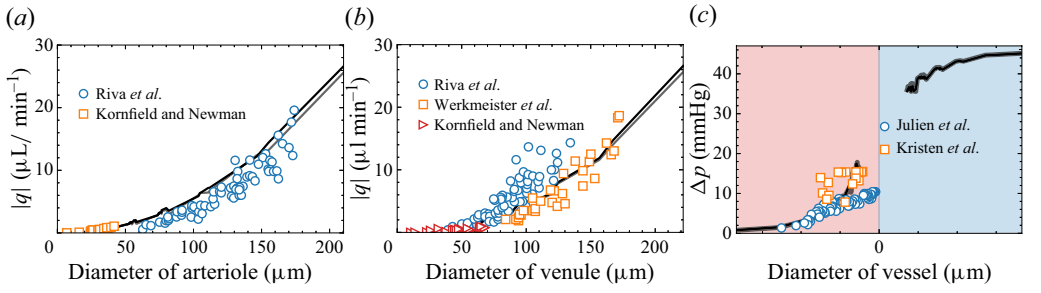


Figure 11. Distributions of flow rate and pressure difference in arterioles and venules. Lines denote the results of multiscale model and markers denote experimental data (Riva *et al.* 1985; Werkmeister *et al.* 2012; Kornfield & Newman 2015) and predictions of other models (Kristen *et al.* 2016; Julien *et al.* 2023). Black and grey lines denote the results with distribution 1 and distribution 2, respectively. (a) Flow rate distributions in arterioles. (b) Flow rate distributions in venules. (c) Pressure difference distributions in arterioles (red region) and venules (blue region). While arteriole diameter decreases from left to right in the red region (from CRA inlet to arterioles near capillary size), venule diameter increases from left to right in the blue region (from venules near capillary size to CRV outlet).

5.1. *Steady flow*

We first explore the dependence of CRA inlet flow rate $q_{in,CRA}$ on the truncation order M, which is shown in figure 10. The value of $q_{in,CRA}$ exhibits convergence for both source distributions when $M > 26$. Besides, the variations are minimal, which are of approximately 2×10^{-4} μl min^{-1} across the entire range of M for both distributions, which is approximately 9×10^{-4} % of total flow (26.61 μl min^{-1} for source distribution 1 and 25.60 μl min^{-1} for source distribution 2). Thus the model could be accurate with only a few terms in the truncation of the series s_1.

Figures 11(a) and 11(b) show the distributions of averaged flow rate along individual arterioles and venules, respectively, where lines denote the results of multiscale model and markers represent experimental data (Riva *et al.* 1985; Werkmeister *et al.* 2012; Kornfield & Newman 2015). Black and grey lines denote the results for source distribution 1 and source distribution 2, respectively, which are almost identical. Our model shows strong agreement with experimental data for arterioles. The flow rates in venules are distributed more sparsely, and our model predictions lie within the observed range of these measurements. The flow rates at CRA inlet and CRV outlet are given in table 2, with a discrepancy of 0.004 μl min^{-1} for both source distributions, which corresponds to approximately 0.013 % of CRA inlet flow rate. Pressure differences Δp between the entry

https://doi.org/10.1017/jfm.2026.11820 Published online by Cambridge University Press

	$q_{in,CRA}$	$p_{in,CRA}$	$q_{out,CRV}$
Steady flow (distribution 1)	26.606 μl min^{-1}	62 mmHg	−26.610 μl min^{-1}
Steady flow (distribution 2)	25.604 μl min^{-1}	62 mmHg	−25.607 μl min^{-1}
Pulsatile flow	26.951 μl min^{-1}	62.188 mmHg	−26.968 μl min^{-1}

Table 2. The flow rates and pressures at CRV outlet and CRA inlet.

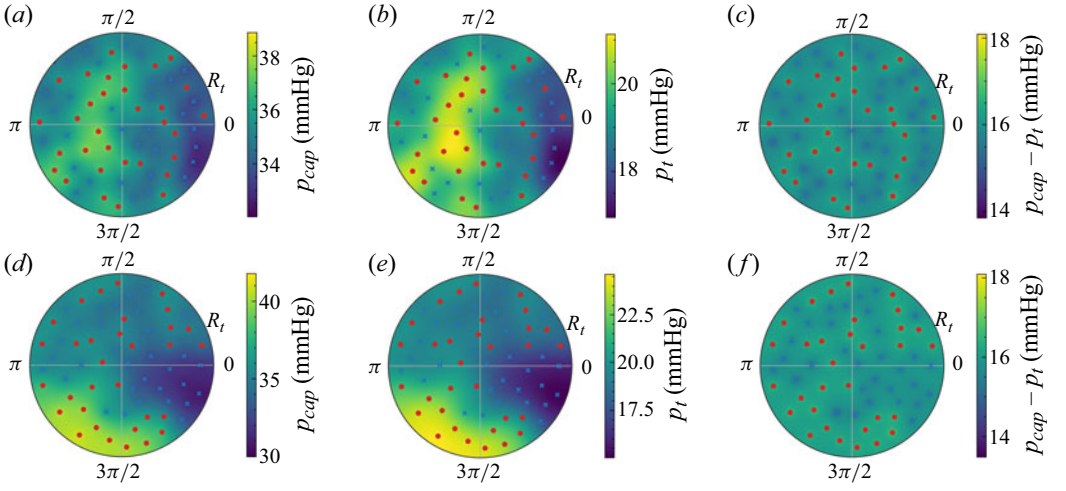


Figure 12. Capillary pressure, tissue pressure and the difference between them. The first row corresponds to source distribution 1 while the second row corresponds to source distribution 2. The red circles and blue crosses denote the sources and sinks, respectively. (*a, d*) Capillary pressures. (*b, e*) Tissue pressures. (*c, f*) Pressure differences.

of CRA and the individual vessel outlets are shown in figure 11(*c*). Results for arterioles and venules are displayed in red and blue regions, respectively, with markers denoting the numerical data from other models (Kristen *et al.* 2016; Julien *et al.* 2023). In the red region, arteriole diameter decreases from left to right, whereas in the blue region, venule diameter increases from left to right. The decrease in pressure across arteriolar tree is approximately 20 mmHg which is greater than that across venules, at approximately 16 mmHg. Our model agrees well with the 3-D model for arteriolar diameter below 60 μm, and with established 1-D model for larger arterioles.

Figures 12(*a*), 12(*b*) and 12(*c*) display the capillary pressure, tissue pressure and their difference for source distribution 1, respectively, while those for distribution 2 are shown in figures 12(*d*), 12(*e*) and 12(*f*). The red circles and blue crosses denote the positions of arteriolar outlets and venular inlets, respectively. The capillary pressure field varies between 32 and 38 mmHg for distribution 1, while for distribution 2 it varies between 30 and 41 mmHg. The tissue pressure field varies between 14 and 18 mmHg for distribution 1, while for distribution 2 it varies between 14 and 23.5 mmHg. The pressure fields for two source distributions differ substantially. However, the capillary pressure is locally larger than the tissue pressure at each point, which results in the positive pressure difference in the entire tissue domain. Moreover, the magnitude of tissue pressure is consistently correct, being slightly above or below IOP. Thus, our model provides a physiologically accurate description for the capillary and tissue pressure.

https://doi.org/10.1017/jfm.2026.11820 Published online by Cambridge University Press

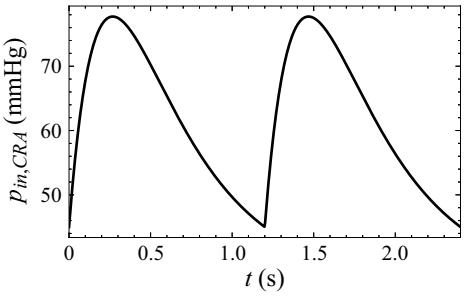


Figure 13. Pulsatile pressure profile at CRA inlet.

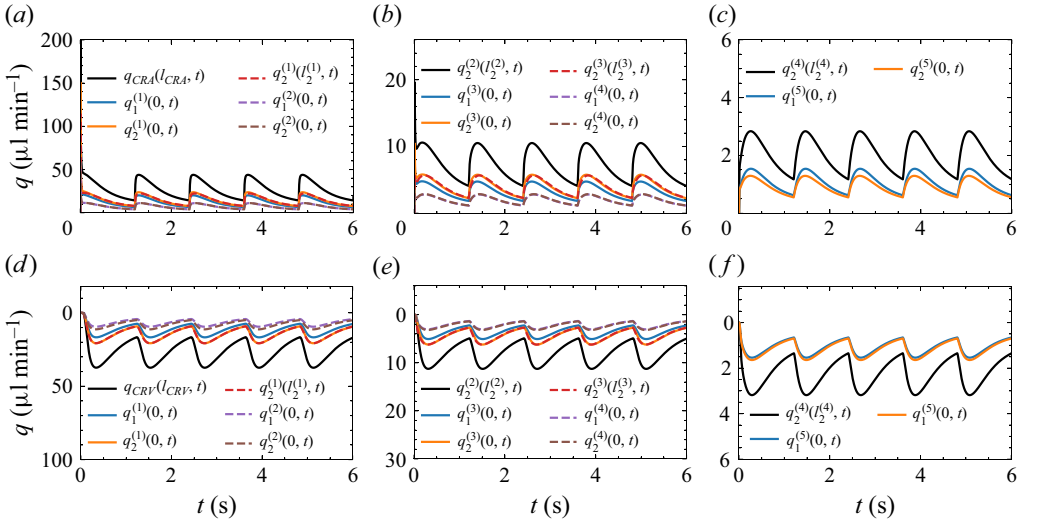


Figure 14. Temporal evolutions of flow rate at bifurcation boundaries of arteriolar and venular trees. (*a–c*) Temporal evolutions of flow rates in arteriolar tree. (*d–f*) Temporal evolutions of flow rates in venular tree.

Table 2 summarises the flow rate and pressure at CRA inlet and CRV outlet. For both source distributions, the flow rate at the CRA inlet is nearly identical to that at the CRV outlet, with a small difference of 0.01 μl min^{-1}.

5.2. *Pulsatile flow*

The CRA inlet pressure could exhibit significant variation due to cardiac pulsation, while the CRV outlet pressure remains almost constant (Guidoboni *et al.* 2014*b*). We next explore the retinal haemodynamics with pulsatile arteriolar pressure at CRA inlet. A cardiac-cycle period of $T = 1.2$ is adopted, with peak systolic pressure at $t_p = 0.268$ s. In the first period, the variation profile is constructed using a shifted function $t\exp(-3.6t)$, whose shape is similar to a pulse profile (Song *et al.* 2024). The waveform is scaled to produce physiologically relevant values: average pressure of 62.16 mmHg approximately, with systolic and diastolic pressures of 77 and 45 mmHg, respectively. The pressure profile at CRA inlet is shown in figure 13.

Figure 14 shows the temporal evolution of flow rate at bifurcation boundaries in arteriolar and venular trees. The flow rates of vessels are denoted as $q_k^{(n)}$, where n is the level of bifurcation boundary and $k = 1, 2$ indicates the daughter vessel index, with their

https://doi.org/10.1017/jfm.2026.11820 Published online by Cambridge University Press

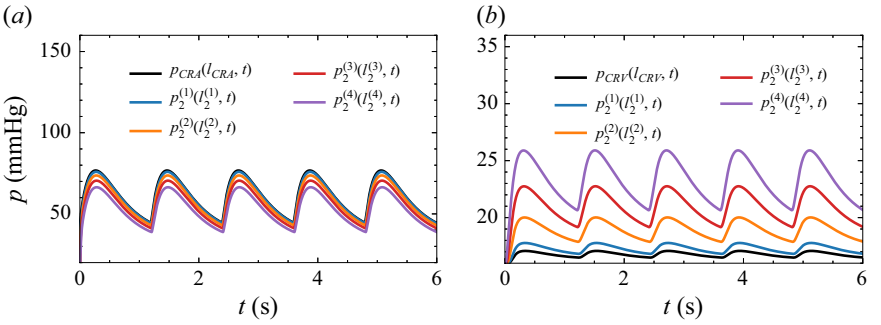


Figure 15. Temporal evolutions of pressure at bifurcation boundaries of arteriolar and venular trees. (*a*) Temporal evolutions of pressures in arteriolar trees; (*b*) temporal evolutions of pressures in venular tree.

lengths following similar notation. Figures 14(*a*), 14(*b*) and 14(*c*) show the flow through the hierarchy of arteriolar bifurcations. In figure 14(*a*), solid lines show the flow rates at first-level bifurcation, including $q_{CRA}(l_{CRA}, t)$ for CRA and $q_1^{(1)}(0, t)$ and $q_2^{(1)}(0, t)$ for its two daughter arterioles, while dashed lines denote the second-level flows from the secondary daughter arteriole in the first-level bifurcation. Figure 14(*b*) advances to third-level flows (solid lines) and fourth-level flows (dashed lines) from the secondary branch in the upper level bifurcation. Figure 14(*c*) displays flow rates at fifth-level bifurcation. The evolution of flow rate in venules is shown in figure 14(*d–f*), following the same descending order as that for arterioles. Flows in both CRA and CRV exhibit initial transients. Arteriolar flows all show pulsatile oscillations similar to the CRA inlet pressure, but with different amplitudes of variations, while venular flows follow similar pulsatility but with negative values indicating flow direction. The variation is largest in the CRA, secondary in the CRV, and becomes dampened in distal arterioles and venules, with minimal oscillation at the fifth-level bifurcations.

Figure 15 shows the temporal evolution of the pressure in these vessels. Since vessels connected to the same bifurcation boundary have identical pressure, only the pressures in mother vessels at each bifurcation are shown. The variation of CRA is largest, and that of CRV is smallest. The pressure waveforms in venules are more distorted than in arterioles. Moreover the pressure amplitude is generally larger in arterioles than in venules, which results from the greater wall stiffness of arterioles.

The flow rates and pressures shown in figures 14 and 15 are averaged and compared with those in steady flow. Figure 16(*a*) shows the mean arteriolar and venular flow rates, denoted by blue and orange markers, respectively. The flow rate distributions for arterioles and venules in steady flow are displayed in blue and orange lines, respectively. The mean arteriolar and venular flows under pulsatile conditions closely match the solutions in steady flow, which results from the longer diastolic phase as well as the time-averaged CRA inlet pressure that is nearly identical to the constant CRA inlet pressure in steady flow. Figures 16(*b*) and 16(*c*) show the systolic pressure (SP), diastolic pressure (DP) and mean pressure $\overline{p}$ as functions of the diameter in arterioles and venules, respectively. The SP, DP and mean pressure are denoted by blue, orange and red markers, respectively. As a baseline, the pressure distribution under constant CRA inlet pressure $p_{in,CRA} = 62$ mmHg is shown by the black line. In steady and pulsatile flows all arteriolar pressures generally increase with diameter but non-monotonically, which indicates the dependence of pressures not only on the diameter but also on the distance from the CRA inlet (Julien *et al.* 2023). Venular pressures decrease with diameter and the decreasing magnitude is

https://doi.org/10.1017/jfm.2026.11820 Published online by Cambridge University Press

	$q^0_{in,CRA}$	$\langle p^0_{cap}\rangle$	$\langle p^0_t\rangle$
Source distribution 1	26.606 μl min^{-1}	34.609 mmHg	18.609 mmHg
Source distribution 2	25.604 μl min^{-1}	36.843 mmHg	20.843 mmHg

Table 3. Baseline values of variables in sensitivity analysis.

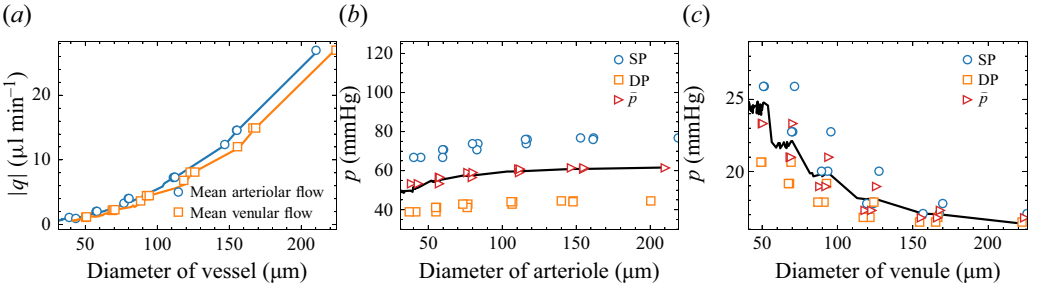


Figure 16. Pulsatile flow rates and pressures as functions of vessel diameter. (*a*) Averaged pulsatile flow rates. The mean arteriolar and venular flows are denoted by blue and orange markers, respectively, while the distributions in steady flow are denoted by solid lines. (*b, c*) Arteriolar and venular pressures. Here, SP, DP and mean pressure are denoted by blue, orange and red markers, respectively, and the pressure distribution with constant CRA inlet pressure is denoted by black line.

smaller than the increasing magnitude in arterioles. Moreover, both arteriolar and venular pressures align closely with corresponding steady distributions.

Table 2 summarises the averaged flow rate and pressure at CRA inlet and CRV outlet. The magnitudes of averaged flow rates at both CRA inlet and CRV outlet are slightly larger than in steady condition due to the higher time-averaged CRA inlet pressure. The flow rates at CRA inlet and CRV outlet are almost identical, and thus the conservation of mass is also satisfied.

6. Sensitivity analysis of parameters in coupled system

We next perform sensitivity analysis of the crucial parameters in capillary–tissue coupled system, including capillary permeability k_{cap}, tissue permeability k_t and exchange rate α_{exch}. To quantify the sensitivity, we use the CRA inlet flow rate $q_{in,CRA}$ as an indicator for vascular trees and the domain-averaged pressures $\langle p_{cap}\rangle$ and $\langle p_t\rangle$ as indicators for the capillary–tissue system, given by (3.72) and (3.73). The oncotic pressure difference is not explored in this section, since the dependence of these variables on it is simple: the CRA inlet flow rate is insensitive to it, as rationalised in § 4.2.2, and it only adds a constant offset to capillary and tissue pressures. The results of $q_{in,CRA}$, $\langle p_{cap}\rangle$ and $\langle p_t\rangle$ for baseline values are denoted by $q^0_{in,CRA}$, $\langle p^0_{cap}\rangle$ and $\langle p^0_t\rangle$, respectively, which are summarised in table 3.

For each parameter analysed, the other two parameters are fixed at their baseline values. Since k_{cap}, k_t and α_{exch} are effective parameters and direct experimental data precisely related to them are scarce, we adopt a prudent approach by allowing these parameters to vary over several orders of magnitude, which correspond to a 99 % decrease and a 9900 % increase, respectively, relative to the baseline value. This enables a comprehensive sensitivity analysis that spans the full range of plausible values and identifies the regimes where they affect the retinal haemodynamics significantly. The baseline values for these three parameters and the rationale for them are provided in Appendix E. The remaining

https://doi.org/10.1017/jfm.2026.11820 Published online by Cambridge University Press

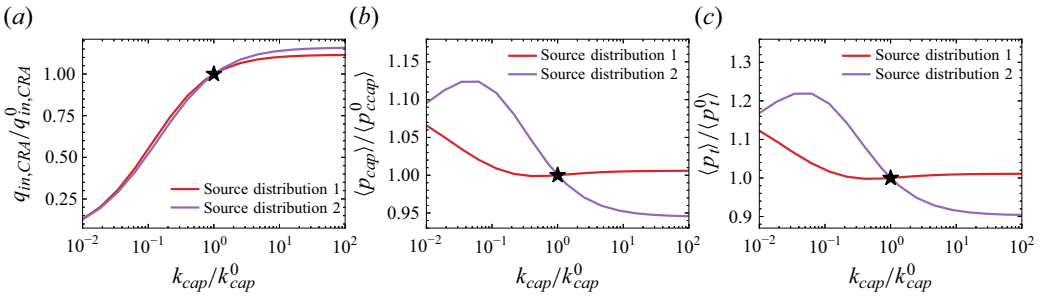


Figure 17. Sensitivity of CRA inlet flow rate and domain-averaged pressures to capillary permeability. The asterisk marker denotes the baseline value. (*a*) Sensitivity of CRA inlet flow rate to capillary permeability. (*b*) Sensitivity of domain-averaged capillary pressure to capillary permeability. (*c*) Sensitivity of domain-averaged tissue pressure to capillary permeability.

parameters, including those in the 1-D model, viscosities μ_{cap} and μ_t and the radius of tissue domain R_t, are summarised in table 1.

6.1. *Sensitivity of capillary permeability*

The effective permeability of capillary bed k_{cap} governs the resistance to flow through the capillaries. We perform a sensitivity analysis over a plausible range to identify the regimes where k_{cap} could significantly affect the retinal haemodynamics. The baseline value is $k^0_{cap} = 0.03\ \mu\text{m}^2$.

Figure 17(*a*) illustrates the sensitivity of CRA inlet flow rate $q_{in,CRA}$ to capillary permeability, where the results for distribution 1 and distribution 2 are denoted by red and purple lines, respectively. For both source distributions, $q_{in,CRA}$ is asymmetrically sensitive to capillary permeability. Decreasing k_{cap} to 1 % of its baseline value decreases flow by approximately 87 %, whereas increasing k_{cap} to 100 times the baseline increases flow by only approximately 11 % and 16 % for source distributions 1 and 2, respectively.

Figures 17(*b*) and 17(*c*) display the sensitivity of domain-averaged capillary pressure $\langle p_{cap}\rangle$ and domain-averaged tissue pressure $\langle p_t\rangle$ to capillary permeability, respectively. For distribution 1, both averaged pressures are higher than their baseline values when k_{cap} is below its baseline, and they increase further as k_{cap} decreases. Above the baseline, pressures saturate around their baseline values. Similarly, for distribution 2, the averaged pressures are higher than their baselines when k_{cap} is below its baseline, but exhibit a non-monotonic dependence on k_{cap}. Above the baseline, $\langle p_{cap}\rangle$ and $\langle p_t\rangle$ tend to approximately 95 % and 90 % of their baseline values, respectively.

These results show that capillary permeability can significantly affect $q_{in,CRA}$, while the variations for $\langle p_{cap}\rangle$ and $\langle p_t\rangle$ across all values of k_{cap} are more modest. Moreover, while capillary and tissue pressures largely depend on the specific source distribution, the flow in arteriolar and venular trees is less sensitive to it.

6.2. *Sensitivity of tissue permeability*

Existing experimental data reveal considerable variation in retinal hydraulic conductivity, spanning two orders of magnitude difference (Fatt & Shantinath 1971; Antcliff 2001; Ruffini *et al.* 2024). Understanding how this variability affects retinal haemodynamics is thus intriguing. The baseline value is $k^0_t = 0.0002\ \mu\text{m}^2$.

Figures 18(*a*), 18(*b*) and 18(*c*) illustrate the sensitivity of CRA inlet flow rate $q_{in,CRA}$, averaged capillary pressure $\langle p_{cap}\rangle$ and averaged tissue pressure $\langle p_t\rangle$ to tissue permeability,

https://doi.org/10.1017/jfm.2026.11820 Published online by Cambridge University Press

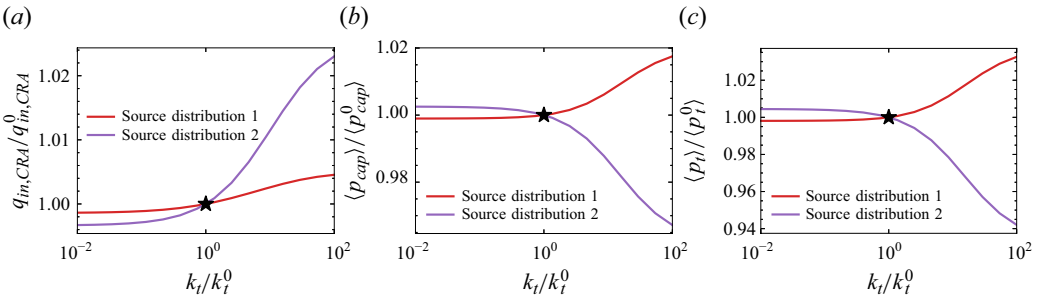


Figure 18. Sensitivity of CRA inlet flow rate and domain-averaged pressures to tissue permeability. The asterisk marker denotes the baseline value. (*a*) Sensitivity of CRA inlet flow rate. (*b*) Sensitivity of domain-averaged capillary pressure. (*c*) Sensitivity of domain-averaged tissue pressure.

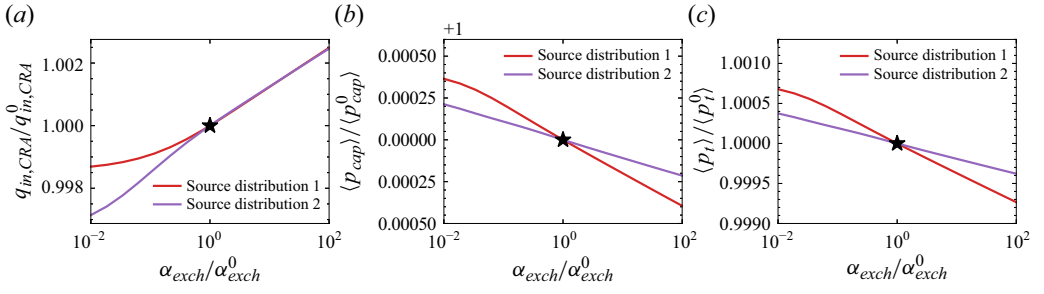


Figure 19. Sensitivity of CRA inlet flow rate and domain-averaged pressures to exchange rate. (*a*) Sensitivity of CRA inlet flow rate. The asterisk marker denotes the baseline value. (*b*) Sensitivity of domain-averaged capillary pressure to exchange rate. (*c*) Sensitivity of domain-averaged tissue pressure to exchange rate.

respectively. The saturation for all three variables occurs below the baseline, with the saturation value at approximately $k_t = 0.0001\ \mu\text{m}^2$. This might suggest that the pathologies affecting tissue permeability would only impair fluid exchange if k_t is below the baseline.

The magnitude of variation for $q_{in,CRA}$ across the full range of k_t is less than 3 % for both source distributions. Moreover, $q_{in,CRA}$ increases as k_t increases for both source distributions. The domain-averaged pressures for the two source distributions exhibit opposite dependencies on k_t: while the pressures for source distribution 1 increase as k_t increases, those for source distribution 2 decrease as k_t increases. The magnitude of variation for both pressures is at most approximately 6 %. Thus all variables are less sensitive to k_t than to k_{cap}. This minimal sensitivity of flow and pressures to tissue permeability indicates that tissue permeability does not play a crucial role in the retinal haemodynamics.

6.3. *Sensitivity of exchange rate*

In our model, the exchange rate $\alpha_{exch} = L_h \times S$ reflects the combined effect of capillary wall hydraulic conductivity L_h and exchange surface area S. An increase in L_h could be related to BRB dysfunction, while a change in S could arise from capillary dilation or pathological angiogenesis.

Figures 19(*a*), 19(*b*) and 19(*c*) show the sensitivity of $q_{in,CRA}$, $\langle p_{cap}\rangle$ and $\langle p_t\rangle$ to α_{exch}, respectively. All three variables are largely insensitive to exchange rate, with very small variations. Specifically, the variation in $q_{in,CRA}$ is the largest at approximately 0.3 %. For both source distributions, $q_{in,CRA}$ increases as α_{exch} increases, and interestingly, the two curves converge to the same value above the baseline α^0_{exch}, showing that $q_{in,CRA}$

https://doi.org/10.1017/jfm.2026.11820 Published online by Cambridge University Press

is independent of the specific distribution of source points above the baseline α^0_{exch}. The domain-averaged pressures increase as α_{exch} decreases. Such insensitivity suggests that although α_{exch} governs local fluid exchange, it has negligible effects on the global hemodynamic variables $q_{in,CRA}$, $\langle p_{cap}\rangle$ and $\langle p_t\rangle$.

7. Discussion and conclusion

This work proposes a multiscale computational model for modelling haemodynamics in retinal microcirculation, by extending previous work on a tree-type vasculature flow model for arterioles and venules and a porous-medium-type model for capillaries and tissue. We have developed a fully coupled flow model that links arterioles, venules, capillaries and interstitial tissue in a unified framework. In particular, the 1-D model (Julien *et al.* 2023) is adopted for the flow of arteriolar and venular trees in the superficial layer, while vessels in the deep layer are modelled as effective resistors. The capillary bed and surrounding tissue are treated as interacting porous media, which are modelled by coupled Darcy models. Our approach is based on widely accepted physical principles, cf. Eisenberg (2023), with necessary simplifications.

Another key novelty of our approach is the derivation and implementation of the analytic solution for capillary–tissue coupled system, which extends previous works that use the analytic solution for capillary flow in multiscale modelling (d'Esposito *et al.* 2018; Shipley *et al.* 2019; Sweeney *et al.* 2024). The capillary–tissue coupled system is solved analytically by using a decoupling transformation, which separates the governing equations into two components, i.e. mean pressure and exchange pressure. The solutions for capillary and tissue pressures are expressed as the combinations of logarithmic functions and infinite series of modified Bessel functions. The convergence and truncation error of infinite series solution are analysed extensively to ensure the robustness and accuracy of the model. This also suggests a potential modelling methodology for other tissues with complicated geometries, where the boundary-sensitive mean pressure could be solved numerically while the exchange pressure, which controls local perfusion, can be effectively approximated using a free-space solution. Furthermore, we establish a dynamic coupling condition that bridges the capillary bed with upstream arteriolar and downstream venular flows. This multiscale coupling, including integral term and nonlinear pressure–area relation, is then simplified for efficient computation.

Our model's predictions with a constant baseline CRA inlet pressure agree well with experimental data, demonstrating its high predictive accuracy. We also simulate the pulsatile flows with a cardiac-cycle pressure profile at the CRA inlet. The results show that the model can characterise pulsations of the pressure and flow in arterioles and venules. Moreover, a sensitivity analysis of the parameters in the capillary–tissue system is performed. The haemodynamics is most sensitive to capillary permeability, followed by tissue permeability and exchange rate, and possible physiological implications are discussed. The flow depends on the specific distribution of source points, and further exploration of how different distributions of source points affect retinal haemodynamics would be valuable. It is also worth noting that saturation occurs when permeabilities move below or above certain values, which might correspond to the lower or upper bound of physiological conditions.

Despite its effectiveness, our model has several limitations. First, we have assumed constant permeabilities for the capillaries and tissue for simplicity, even though we are aware that biology and evolution are likely to use spatially variable permeabilities. Indeed, the type of permeability might be expected to vary from location to location, reflecting the specialised distribution of ion channels and transporters used by evolution to create

https://doi.org/10.1017/jfm.2026.11820 Published online by Cambridge University Press

overall function. Work is currently underway to extend our work to spatially varying permeabilities, which will allow us to explore physiologically relevant questions such as the effect of the non-uniform nature of the capillaries. We are also extending our model to time-varying permeability of the capillaries to explore the effect of neurovascular coupling. Second, we approximate the area where the retinal vasculature is distributed as a 2-D circular domain, and further studies could consider a 3-D spherical geometry, which would represent the actual retinal anatomy better. Additionally, the model does not distinguish different capillary plexuses located in the outer retina and inner retina (Causin *et al.* 2016), and this simplification could be addressed. Notably, several works have developed transport models for water and various organic and inorganic molecules in the optic nerve (Zhu *et al.* 2019, 2021*a*; Zhu *et al.* 2021*b*, *c*; Song *et al.* 2024; Xiao *et al.* 2025*a*,*b*), and several fundamental properties of the transport in optic nerve have been revealed. Combining our multiscale model with such models could provide deeper insights into retinal physiology and pathology. Similarly, adding the active pumping of retinal pigment epithelium and passive exchange with the vitreous chamber will help to describe more physiologically relevant situations. Finally, the boundary condition for tissue pressure enforces no fluid accumulation in the tissue, and it might not be physiologically accurate in certain pathological situations. For example, exudative macular oedema is caused by the fluid accumulation in the tissue (Ruffini *et al.* 2024). Further studies could thus explore other boundary conditions for such pathological situations.

In conclusion, the multiscale model proposed in this work provides an efficient and robust tool for exploring the haemodynamics in retinal microcirculation. Despite the necessary simplifications on which the model is based, our model generates physiologically consistent results and could thus help to understand the mechanisms of retinopathies as well as perform the computation for specific patients.

Acknowledgements. We thank Professor Rongliang Chen and Zhen Zhang for helpful discussions during the early stage of this work.

Funding. This work is supported in part by NSFC (Project number 12231004). We thank the reviewers whose comments motivated significant improvements to the paper.

Declaration of interests. The authors report no conflict of interest.

Appendix A. Solution for mean pressure

Enforcing the boundary $\nabla' f_{mean}(\boldsymbol{x}, \boldsymbol{x}') \cdot \boldsymbol{n}' = 1/(2\pi R_t)$ yields

$$\frac{1}{|\boldsymbol{x}' - \boldsymbol{x}|^2}\left[|\boldsymbol{x}'|^2 + k|\boldsymbol{x}|^2 - (k+1)\boldsymbol{x}' \cdot \boldsymbol{x}\right] = 1, \tag{A1}$$

which holds for all $\boldsymbol{x}$ and $\boldsymbol{x}'$ if and only if $k = 1$, thus the coefficient k is uniquely determined. The constant c remains arbitrary and can be set as $c = 0$ without loss of generality. Thus the solution to the adjoint problem is

$$f_{mean}(\boldsymbol{x}, \boldsymbol{x}') = \frac{1}{2\pi}\left(\log|\boldsymbol{x}' - \boldsymbol{x}| + \log|\boldsymbol{x}' - \boldsymbol{x}''|\right). \tag{A2}$$

Then, the solution for p_{mean} can be obtained via the following convolution (Kim & Jackson 1993; Riley *et al.* 2006):

$$p_{mean} = \int_{\Omega_t} f_{mean} \nabla'^2 p_{mean}(\boldsymbol{x}')\mathrm{d}\boldsymbol{x}' + \int_{\partial\Omega_t}\left[p_{mean}(\boldsymbol{x}')\nabla' f_{mean} - f_{mean}\nabla' p_{mean}(\boldsymbol{x}')\right] \cdot \boldsymbol{n}'\mathrm{d}s'. \tag{A3}$$

https://doi.org/10.1017/jfm.2026.11820 Published online by Cambridge University Press

Substituting the boundary conditions for f_{mean} and p_{mean} yields

$$p_{mean}(\boldsymbol{x}) = \int_{\Omega_t} f_{mean}(\boldsymbol{x}, \boldsymbol{x}')\nabla'^2 p_{mean}(\boldsymbol{x}')\mathrm{d}\boldsymbol{x}' + \frac{1}{S}\int_{\partial\Omega_t} p_{mean}(\boldsymbol{x}')\mathrm{d}s'. \tag{A4}$$

The first integral is computed as

$$\begin{aligned}\int_{\Omega_t} f_{mean}(\boldsymbol{x}, \boldsymbol{x}')\nabla'^2 p_{mean}(\boldsymbol{x}')\mathrm{d}\boldsymbol{x}' &= -\frac{1}{\kappa_{cap}+\kappa_t}\sum_{n=1}^{N_{cap}} q_n \int_{\Omega_t} f_{mean}(\boldsymbol{x}, \boldsymbol{x}')\delta(\boldsymbol{x}' - \boldsymbol{x}_n)\mathrm{d}\boldsymbol{x}' \\ &= -\frac{1}{\kappa_{cap}+\kappa_t}\sum_{n=1}^{N_{cap}} q_n f_{mean}(\boldsymbol{x}, \boldsymbol{x}_n).\end{aligned} \tag{A5}$$

Appendix B. Solution for the Green's function of the exchange pressure

The continuity of the function f_{exch} at $r = r_n$ provides that

$$R_{m,n}(r)|_{r=r_n^+} - R_{m,n}(r)|_{r=r_n^-} = 0, \tag{B1}$$

and the discontinuity of the derivative of f_{exch} implies that

$$\left.\frac{\mathrm{d}R_{m,n}(r)}{\mathrm{d}r}\right|_{r=r_n^+} - \left.\frac{\mathrm{d}R_{m,n}(r)}{\mathrm{d}r}\right|_{r=r_n^-} = \frac{1}{r_n}. \tag{B2}$$

Moreover imposing the no-flux boundary condition yields

$$\left.\frac{\mathrm{d}R_{m,n}(r)}{\mathrm{d}r}\right|_{r=R_t} = 0. \tag{B3}$$

The boundary condition $\mathrm{d}R_{m,n}(r)/\mathrm{d}r|_{r=R_t} = 0$ provides that

$$C_{m,n} = -\frac{I'_m(\lambda R_t)}{K'_m(\lambda R_t)}B_{m,n}, \tag{B4}$$

and the continuity of $R_m(r)$ yields

$$A_{m,n} = \left[1 - \frac{I'_m(\lambda R_t)}{K'_m(\lambda R_t)}\frac{K_m(\lambda r_n)}{I_m(\lambda r_n)}\right]B_{m,n}. \tag{B5}$$

Thus the discontinuity of $\mathrm{d}R_m(r)/\mathrm{d}r$ at $r = r_n$ gives rise to

$$-B_{m,n}\frac{I'_m(\lambda R_t)}{K'_m(\lambda R_t)}\frac{I_m(\lambda r_n)K'_m(\lambda r_n) - K_m(\lambda r_n)I'_m(\lambda r_n)}{I_m(\lambda r_n)} = \frac{1}{\lambda r_n}, \tag{B6}$$

and using the identity (Baricz *et al.* 2016, p. 866)

$$I_m(\lambda r_n)K'_m(\lambda r_n) - K_m(\lambda r_n)I'_m(\lambda r_n) = -\frac{1}{\lambda r_n} \tag{B7}$$

we obtain

$$B_{m,n} = \frac{K'_m(\lambda R_t)}{I'_m(\lambda R_t)}I_m(\lambda r_n), \tag{B8}$$

and

$$A_{m,n} = \frac{K'_m(\lambda R_t)I_m(\lambda r_n)}{I'_m(\lambda R_t)} - K_m(\lambda r_n), \tag{B9}$$

https://doi.org/10.1017/jfm.2026.11820 Published online by Cambridge University Press

$$C_{m,n} = -I_m(\lambda r_n). \tag{B10}$$

Appendix C. Ratio between terms

The ratio between the first term and the second term in the radial component is given by

$$e_{m,n} = \left| \frac{K'_m(\lambda R_t) I_m(\lambda r^n_>)}{I'_m(\lambda R_t) K_m(\lambda r^n_>)} \right|. \tag{C1}$$

If m is fixed, the derivative $K'_m(\lambda r)$ is negative and increasing. Then,

$$e_{m,n} \le -\frac{K'_m(\lambda R_t) I_m(\lambda r^n_>)}{I'_m(\lambda r^n_>) K_m(\lambda r^n_>)}. \tag{C2}$$

Using the inequality that (Baricz *et al.* 2016, p. 867)

$$\frac{I'_m(\lambda r)}{I_m(\lambda r)} > \frac{m}{\lambda r}, \quad m > -1, \quad \lambda r > 0, \tag{C3}$$

the inequality can be written as

$$e_{m,n} \le -\frac{\lambda r^n_>}{m} \frac{K'_m(\lambda R_t)}{K_m(\lambda r^n_>)}, \quad m > -1, \quad \lambda r > 0. \tag{C4}$$

Using the inequality that (Baricz *et al.* 2016, p. 867)

$$-\frac{K'_m(\lambda r)}{K_m(\lambda r)} < \frac{m}{\lambda r} + 1, \quad m > 1/2, \quad \lambda r > 0, \tag{C5}$$

we obtain

$$e_{m,n} \le \frac{\lambda r^n_>}{m} \left(\frac{m}{\lambda R_t} + 1 \right) \frac{K_m(\lambda R_t)}{K_m(\lambda r^n_>)}, \quad m > 1/2, \quad \lambda r > 0. \tag{C6}$$

Using the inequality (Baricz 2010, equation (3.4); Joshi & Bissu 1996, equation (2.17)) that $K_m(r_1)/K_m(r_2) > (r_2/r_1)^m$ for $m > -1/2$ and $0 < r_1 < r_2$, we obtain that

$$e_{m,n} \le \frac{\lambda r^n_>}{m} \left(\frac{m}{\lambda R_t} + 1 \right) \left(\frac{\lambda r^n_>}{\lambda R_t} \right)^m, \quad m > 1/2, \quad \lambda r > 0, \tag{C7}$$

thus for $0 \le r < R_t$ the ratio $e_{m,n} \to 0$ as $m \to \infty$ and the first term can be neglected.

Appendix D. Proof of addition formula for infinite series

Consider the following problem in two dimensions:

$$\nabla^2 f_{exch}(\boldsymbol{x}, \boldsymbol{x}_n) - \lambda^2 f_{exch}(\boldsymbol{x}, \boldsymbol{x}_n) = \delta(\boldsymbol{x} - \boldsymbol{x}_n), \tag{D1}$$

subject to the boundary condition that $f_{exch} \to 0$ as $|\boldsymbol{x}| \to \infty$. In polar coordinates, with $\boldsymbol{x}_n = (r_n, \theta_n)$, the equation is given by (3.29). Expanding f_{exch} in a Fourier series and solving the resulting modified Bessel equation, with proper matching for the coefficients of the expansion of the delta function, yields

$$f_{exch} = -\frac{1}{2\pi} \sum_{m=-\infty}^{\infty} I_m(\lambda r_<) K_m(\lambda r_>) \exp[im(\theta - \theta_n)], \tag{D2}$$

https://doi.org/10.1017/jfm.2026.11820 Published online by Cambridge University Press

and $r_<^n = \min(r, r_n)$ and $r_>^n = \max(r, r_n)$. On the other hand, by translational and rotational invariance of the infinite-domain problem, f_{exch} depends only on the distance $\xi_n = |\boldsymbol{x} - \boldsymbol{x}_n|$. The equation becomes

$$\frac{1}{\xi_n}\frac{\partial}{\partial \xi_n}\left(\xi_n \frac{\partial f_{exch}}{\partial \xi_n}\right) - \lambda^2 f_{exch} = \frac{\delta(\xi_n)}{2\pi \xi_n}, \tag{D3}$$

and solving this equation with the given boundary condition we obtain

$$f_{exch} = -\frac{1}{2\pi} K_0\left(\lambda\sqrt{r^2 + r_n^2 - 2rr_n\cos(\theta - \theta_n)}\right). \tag{D4}$$

Then the uniqueness of the solution implies the addition formula for modified Bessel functions.

Appendix E. Range of parameters in coupled system

The effective permeability of the capillary bed in porous medium models varies across different tissues. In previous work on retinal haemodynamics, a hydraulic conductivity of $0.1\,\mathrm{mm}^2\,(\mathrm{s\,kPa})^{-1}$ was used in the Darcy model for retinal capillaries (Dziubek *et al.* 2016), which yields $k_{cap} \approx 0.3\,\mu\mathrm{m}^2$ using a blood viscosity $\mu_{cap} \approx 3\,\mathrm{cP}$. We adopt a moderate capillary permeability $k_{cap}^0 = 0.03\,\mu\mathrm{m}^2$ for a baseline value and consider a plausible range from $k_{cap} = 0.0003\,\mu\mathrm{m}^2$ to $k_{cap} = 3\,\mu\mathrm{m}^2$.

For the interstitial fluid in tissue, clinical observations provide sparse values spanning two orders of magnitude difference. The hydraulic conductivity in a human retina is $2.54 \times 10^{-10}\,\mathrm{m\,s^{-1}\,Pa^{-1}}$ (Antcliff 2001; Ruffini *et al.* 2024), which corresponds to an intrinsic permeability of approximately $6 \times 10^{-5}\,\mu\mathrm{m}^2$ with a fluid viscosity $\mu_t = 0.7\,\mathrm{cP}$. Moreover the range of tissue permeabilities extends to approximately of the order of $10^{-2}\,\mu\mathrm{m}^2$ (Fatt & Shantinath 1971). Given this variation, the baseline tissue permeability is then set as $k_t^0 = 0.0002\,\mu\mathrm{m}^2$, with a plausible range from 2×10^{-6} to $0.02\,\mu\mathrm{m}^2$.

The exchange rate between capillaries and tissue α_{exch} depends on capillary wall hydraulic conductivity L_h and the exchange surface area per unit tissue volume S. Given that retinal capillaries are fundamentally similar in barrier structure to those in brain (Bradbury & Lightman 1990), we use the value of hydraulic conductivity $L_h = 0.2 \times 10^{-7}\,\mathrm{cm\,s^{-1}\,cm^{-1}\,H_2O^{-1}}$ from clinical observations for human brain (Helton *et al.* 2017). Considering the characteristic capillary radius $6\,\mu\mathrm{m}$ and the volume fraction 1 %, then $S \approx 30\,\mathrm{cm}^{-1}$ which yields a value $\alpha_{exch} \approx 6.1 \times 10^{-6}\,\mu\mathrm{m\,s\,g^{-1}}$. We then adopt a moderate value $\alpha_{exch}^0 = 0.0002\,\mu\mathrm{m\,s\,g^{-1}}$ for baseline value and a plausible range of α_{exch} from $\alpha_{exch} = 2 \times 10^{-6}\,\mu\mathrm{m\,s\,g^{-1}}$ to $\alpha_{exch} = 0.02\,\mu\mathrm{m\,s\,g^{-1}}$.

References

Abramowitz, M. & Stegun, I.A. 2013 *Handbook of Mathematical Functions: with Formulas, Graphs, and Mathematical Tables*, 9th edn. Dover Publications.

Antcliff, R.J. 2001 Hydraulic conductivity of fixed retinal tissue after sequential excimer laser ablation: barriers limiting fluid distribution and implications for cystoid macular edema. *Arch. Ophthalmol.* **119** (4), 539.

Arichika, S., Uji, A., Ooto, S., Muraoka, Y. & Yoshimura, N. 2015 Effects of age and blood pressure on the retinal arterial wall, analyzed using adaptive optics scanning laser ophthalmoscopy. *Sci. Rep.* **5** (1), 12283.

Audebert, C., Bucur, P., Bekheit, M., Vibert, E., Vignon-Clementel, I.E. & Gerbeau, J.-F. 2017 Kinetic scheme for arterial and venous blood flow, and application to partial hepatectomy modeling. *Comput. Meth. Appl. Mech. Engng* **314**, 102–125.

https://doi.org/10.1017/jfm.2026.11820 Published online by Cambridge University Press

Bappoo, N., Kelsey, L.J., Parker, L., Crough, T., Moran, C.M., Thomson, A., Holmes, M.C., Wyrwoll, C.S. & Doyle, B.J. 2017 Viscosity and haemodynamics in a late gestation rat feto-placental arterial network. *Biomech. Model. Mechanobiol.* **16** (4), 1361–1372.

Baricz, Á. 2010 Bounds for modified Bessel functions of the first and second kinds. *Proc. Edin. Math. Soc.* **53** (3), 575–599.

Baricz, Á., Maširević, D.J., Ponnusamy, S. & Singh, S. 2016 Bounds for the product of modified Bessel functions. *Aequationes Mathematicae* **90** (4), 859–870.

Bradbury, M.W.B. & Lightman, S.L. 1990 The blood-brain interface. *Eye* **4** (2), 249–254.

Brown, E.E. *et al.* 2024 Physics-informed deep generative learning for quantitative assessment of the retina. *Nat. Commun.* **15** (1), 6859.

Caprioli, J. & Coleman, A.L. 2010 Blood pressure, perfusion pressure, and glaucoma. *Am. J. Ophthalmol.* **149** (5), 704–712.

Causin, P., Guidoboni, G., Malgaroli, F., Sacco, R. & Harris, A. 2016 Blood flow mechanics and oxygen transport and delivery in the retinal microcirculation: multiscale mathematical modeling and numerical simulation. *Biomech. Model. Mechanobiol.* **15** (3), 525–542.

Ch'ng, T.W., Chua, C.Y., Ummi Kalsom, M.A., Azhany, Y., Gong, V.H.M., Rasool, A.H.G. & Liza-Sharmini, A.T. 2021 Ocular perfusion pressure and severity of glaucoma: is there a link? *J. Curr. Glaucoma Practice* **15** (2), 78–85.

d'Esposito, A. *et al.* 2018 Computational fluid dynamics with imaging of cleared tissue and of in vivo perfusion predicts drug uptake and treatment responses in tumours. *Nat. Biomed. Engng* **2** (10), 773–787.

Dorner, G.T., Polska, E., Garhöfer, G., Zawinka, C., Frank, B. & Schmetterer, L. 2002 Calculation of the diameter of the central retinal artery from noninvasive measurements in humans. *Curr. Eye Res.* **25** (6), 341–345.

Dvoriashyna, M., Foss, A.J.E., Gaffney, E.A., Jensen, O.E. & Repetto, R. 2018 Osmotic and electroosmotic fluid transport across the retinal pigment epithelium: a mathematical model. *J. Theor. Biol.* **456**, 233–248.

Dziubek, A., Guidoboni, G., Harris, A., Hirani, A.N., Rusjan, E. & Thistleton, W. 2016 Effect of ocular shape and vascular geometry on retinal hemodynamics: a computational model. *Biomech. Model. Mechanobiol.* **15** (4), 893–907.

Eisenberg, R. 2023 Structural analysis of fluid flow in complex biological systems. *Model. Artif. Intell. Ophthalmol.* **4** (1), 1–12.

Ertop, M., Fulya, Y.T., Aribaş, Y.K., Özdemir, H.B., Gürelik, G., Atilgan, M.E. & Özdek, Ş. 2023 Evaluation of central and peripheral retinal vascular changes in the fellow eyes of patients with unilateral retinal vein occlusions. *Turkish J. Ophthalmol.* **53** (6), 349–355.

Fatt, I. & Shantinath, K. 1971 Flow conductivity of retina and its role in retinal adhesion. *Exp. Eye Res.* **12** (2), 218–226.

Ferrara, M., Lugano, G., Sandinha, M.T., Kearns, V.R., Geraghty, B. & Steel, D.H.W. 2021 Biomechanical properties of retina and choroid: a comprehensive review of techniques and translational relevance. *Eye* **35** (7), 1818–1832.

Flores, J., Alastruey, J. & Corvera Poiré, E. 2016 A novel analytical approach to pulsatile blood flow in the arterial network. *Ann. Biomed. Engng* **44** (10), 3047–3068.

Fritz, M., Köppl, T., Oden, J., Wagner, A., Wohlmuth, B. & Wu, C. 2022 A 1D–0D–3D coupled model for simulating blood flow and transport processes in breast tissue. *Intl J. Numer. Meth. Biomed. Engng* **38** (7), e3612.

Fry, B.C., Coburn, E.B., Whiteman, S., Harris, A., Siesky, B. & Arciero, J. 2018 Predicting retinal tissue oxygenation using an image-based theoretical model. *Math. Biosci.* **305**, 1–9.

Ganesan, P., He, S. & Xu, H. 2010 Analysis of retinal circulation using an image-based network model of retinal vasculature. *Microvasc. Res.* **80** (1), 99–109.

Garhöfer, G., Zawinka, C., Resch, H., Huemer, K.H., Schmetterer, L. & Dorner, G.T. 2004 Response of retinal vessel diameters to flicker stimulation in patients with early open angle glaucoma. *J. Glaucoma* **13** (4), 340–344.

Gradshteĭn, I.S. & Zwillinger, D. 2015 *Table of Integrals, Series, and Products*, 8th edn. Elsevier, Academic Press is an imprint of Elsevier.

Guidoboni, G., Harris, A., Carichino, L., Arieli, Y. & Siesky, B.A. 2014*a* Effect of intraocular pressure on the hemodynamics of the central retinal artery: a mathematical model. *Math. Biosci. Engng* **11** (3), 523–546.

Guidoboni, G., Harris, A., Cassani, S., Arciero, J., Siesky, B., Amireskandari, A., Tobe, L., Egan, P., Januleviciene, I. & Park, J. 2014*b* Intraocular pressure, blood pressure, and retinal blood

https://doi.org/10.1017/jfm.2026.11820 Published online by Cambridge University Press

flow autoregulation: a mathematical model to clarify their relationship and clinical relevance. *Investigative Opthalmol. Vis. Sci.* **55** (7), 4105.

He, Y., Liu, H. & Himeno, R. 2004 A one-dimensional thermo-fluid model of blood circulation in the human upper limb. *Intl J. Heat Mass Transfer* **47** (12–13), 2735–2745.

Helton, E.S., Palladino, S. & Ubogu, E.E. 2017 A novel method for measuring hydraulic conductivity at the human blood-nerve barrier in vitro. *Microvasc. Res.* **109**, 1–6.

Hernandez, R.J., Madhusudhan, S., Zheng, Y. & El-Bouri, W.K. 2024 Linking vascular structure and function: image-based virtual populations of the retina. *Investigative Ophthalmol. Vis. Sci.* **65** (4), 40.

Joshi, C.M. & Bissu, S.K. 1996 Inequalities for some special functions. *J. Comput. Appl. Maths* **69** (2), 251–259.

Józsa, T.I., Padmos, R.M., Samuels, N., El-Bouri, W.K., Hoekstra, A.G. & Payne, S.J. 2021 A porous circulation model of the human brain for *in silico* clinical trials in ischaemic stroke. *Interface Focus* **11** (1), 20190127.

Julien, L., Bonnin, S., Paques, M. & Fullana, J.-M. 2023 One-dimensional modeling of microvascular hemodynamics in the retina using multimodal imaging. *Phys. Fluids* **35** (6), 061901.

Kiel, J.W. 2011 The ocular circulation. *Colloquium Ser. Integrated Syst. Physiol.: Molecule Func.* **3** (1), 1–81.

Kim, K.J. & Jackson, J.D. 1993 Proof that the Neumann Green's function in electrostatics can be symmetrized. *Am. J. Phys.* **61** (12), 1144–1146.

Kolachalama, V.B., Bressloff, N.W., Nair, P.B. & Shearman, C.P. 2007 Predictive haemodynamics in a one-dimensional human carotid artery bifurcation. Part I: application to stent design. *IEEE Trans. Biomed. Engng* **54** (5), 802–812.

Köppl, T. & Helmig, R. 2023 *Dimension Reduced Modeling of Blood Flow in Large Arteries: an Introduction for Master Students and First Year Doctoral Students*. Springer International Publishing.

Kornfield, T.E. & Newman, E.A. 2015 Measurement of retinal blood flow using fluorescently labeled red blood cells. *eNeuro* **2** (2), ENEURO.0005-15.2015.

Kristen, A., Kelsey, L., Wintermantel, E. & Doyle, B. 2016 Fundus image based blood flow simulation of the retinal arteries. In *Computational Biomechanics for Medicine* (ed. G.R. Joldes, B. Doyle, A. Wittek, P.M.F. Nielsen & K. Miller), pp. 143–154. Springer International Publishing.

Liu, D., Wood, N.B., Witt, N., Hughes, A.D., Thom, S.A. & Xu, X.Y. 2009 Computational analysis of oxygen transport in the retinal arterial network. *Curr. Eye Res.* **34** (11), 945–956.

Liu, J. & Suito, H. 2024 A multicore parallel algorithm for multiscale modelling of an entire human blood circulation network. ArXiv: 2404.01680.

Malek, J., Azar, A.T., Nasralli, B., Tekari, M., Kamoun, H. & Tourki, R. 2015 Computational analysis of blood flow in the retinal arteries and veins using fundus image. *Comput. Maths Applics.* **69** (2), 101–116.

Morissette, M.P. 1977 Colloid osmotic pressure: its measurement and clinical value. *Can. Med. Assoc. J.* **116** (8), 897–900.

Müller, L.O. & Toro, E.F. 2014 A global multiscale mathematical model for the human circulation with emphasis on the venous system: a global multiscale mathematical model for the human circulation. *Intl J. Numer. Meth. Biomed. Engng* **30** (7), 681–725.

Olufsen, M.S., Peskin, C.S., Kim, W.Y., Pedersen, E.M., Nadim, A. & Larsen, J. 2000 Numerical simulation and experimental validation of blood flow in arteries with structured-tree outflow conditions. *Ann. Biomed. Engng* **28** (11), 1281–1299.

Osborne, N.N., Casson, R.J., Wood, J.P.M., Chidlow, G., Graham, M. & Melena, J. 2004 Retinal ischemia: mechanisms of damage and potential therapeutic strategies. *Prog. Retinal Eye Res.* **23** (1), 91–147.

Pries, A.R., Secomb, T.W., Gessner, T., Sperandio, M.B., Gross, J.F. & Gaehtgens, P. 1994 Resistance to blood flow in microvessels in vivo. *Circulation Res.* **75** (5), 904–915.

Qohar, U.N.A., Munthe-Kaas, A.Z., Nordbotten, J.M. & Hanson, E.A. 2021 A nonlinear multi-scale model for blood circulation in a realistic vascular system. *R. Soc. Open Sci.* **8** (12), 201949.

Rebhan, J., Parker, L.P., Kelsey, L.J., Chen, F.K. & Doyle, B.J. 2019 A computational framework to investigate retinal haemodynamics and tissue stress. *Biomech. Model. Mechanobiol.* **18** (6), 1745–1757.

Riley, K.F., Hobson, M.P. & Bence, S.J. 2006 *Mathematical Methods for Physics and Engineering*, 3rd edn. Cambridge University Press.

Riva, C.E., Grunwald, J.E., Sinclair, S.H. & Petrig, B.L. 1985 Blood velocity and volumetric flow rate in human retinal vessels. *Investigative Ophthalmol. Vis. Sci.* **26** (8), 1124–1132.

Ruffini, A., Dvoriashyna, M., Govetto, A., Romano, M.R. & Repetto, R. 2024 A mathematical model of interstitial fluid flow and retinal tissue deformation in macular edema. *Investigative Ophthalmol. Vis. Sci.* **65** (11), 19.

https://doi.org/10.1017/jfm.2026.11820 Published online by Cambridge University Press

RUIZ-ANTOLÍN, D. & SEGURA, J. 2016 A new type of sharp bounds for ratios of modified Bessel functions. *J. Math. Anal. Applics.* **443** (2), 1232–1246.

SECOMB, T.W. & PRIES, A.R. 2013 Blood viscosity in microvessels: experiment and theory. *C. R. Phys.* **14** (6), 470–478.

SHIPLEY, R.J., SMITH, A.F., SWEENEY, P.W., PRIES, A.R. & SECOMB, T.W. 2019 A hybrid discrete–continuum approach for modelling microcirculatory blood flow. *Math. Med. Biol.* **37** (1), 40–57.

SIGGERS, J.H. & ETHIER, C.R. 2012 Fluid mechanics of the eye. *Annu. Rev. Fluid Mech.* **44** (1), 347–372.

SONG, W., WEI, Q., LIU, W., LIU, T., YI, J., SHEIBANI, N., FAWZI, A.A., LINSENMEIER, R.A., JIAO, S. & ZHANG, H.F. 2014 A combined method to quantify the retinal metabolic rate of oxygen using photoacoustic ophthalmoscopy and optical coherence tomography. *Sci. Rep.* **4** (1), 6525.

SONG, Z., XU, S., EISENBERG, R. & HUANG, H. 2024 A multi-domain model for microcirculation in optic nerve: blood flow and oxygen transport. *Phys. D* **467**, 134272.

STAAL, J., ABRAMOFF, M.D., NIEMEIJER, M., VIERGEVER, M.A. & VAN GINNEKEN, B. 2004 Ridge-based vessel segmentation in color images of the retina. *IEEE Trans. Med. Imaging* **23** (4), 501–509.

SWEENEY, P.W., WALSH, C., WALKER-SAMUEL, S. & SHIPLEY, R.J. 2024 A three-dimensional, discrete-continuum model of blood pressure in microvascular networks. *Intl J. Numer. Meth. Biomed. Engng* **40** (8), e3832.

TRIPATHY, K.C., SIDDHARTH, A. & BHANDARI, A. 2023 Image-based insilico investigation of hemodynamics and biomechanics in healthy and diabetic human retinas. *Microvasc. Res.* **150**, 104594.

TRUSKEY, G.A., FAN, Y. & KATZ, D.F. 2009 *Transport Phenomena in Biological Systems*, 2nd edn. Pearson Prentice Hall.

VIDOTTO, E., KOCH, T., KÖPPL, T., HELMIG, R. & WOHLMUTH, B. 2019 Hybrid models for simulating blood flow in microvascular networks. *Multiscale Model. Simul.* **17** (3), 1076–1102.

WANG, X.-F., NISHI, S., MATSUKAWA, M., GHIGO, A., LAGRÉE, P.-Y. & FULLANA, J.-M. 2016 Fluid friction and wall viscosity of the 1D blood flow model. *J. Biomech.* **49** (4), 565–571.

WERKMEISTER, R.M., DRAGOSTINOFF, N., PALKOVITS, S., TOLD, R., BOLTZ, A., LEITGEB, R.A., GRÖSCHL, M., GARHÖFER, G. & SCHMETTERER, L. 2012 Measurement of absolute blood flow velocity and blood flow in the human retina by dual-beam bidirectional Doppler Fourier-domain optical coherence tomography. *Investigative Opthalmol. Vis. Sci.* **53** (10), 6062.

XIAO, S., HUANG, H., EISENBERG, R., SONG, Z. & XU, S. 2025*a* Glymphatic clearance in the optic nerve: a multidomain electro-osmostic model. ArXiv: 2510.22271.

XIAO, S., HUANG, H., EISENBERG, R., SONG, Z. & XU, S. 2025*b* Potassium clearance in optic nerve: a multidomain model. *Frontiers Biosci. (Landmark Ed)* **30** (7), 39722.

XU, S., EISENBERG, B., SONG, Z. & HUANG, H. 2018 Osmosis through a Semi-Permeable Membrane: a Consistent Approach to Interactions. Arxiv:1806.00646.

ZAMIR, M. 2001 Arterial branching within the confines of fractal L-system Formalism. *J. Gen. Physiol.* **118** (3), 267–276.

ZHU, Y., XU, S., EISENBERG, R.S. & HUANG, H. 2019 A bidomain model for lens microcirculation. *Biophys. J.* **116** (6), 1171–1184.

ZHU, Y., XU, S., EISENBERG, R.S. & HUANG, H. 2021*a* Membranes in optic nerve models. ArXiv.2105.14411.

ZHU, Y., XU, S., EISENBERG, R.S. & HUANG, H. 2021*b* Optic nerve microcirculation: fluid flow and electrodiffusion. *Phys. Fluids* **33** (4), 041906.

ZHU, Y., XU, S., EISENBERG, R.S. & HUANG, H. 2021*c* A tridomain model for potassium clearance in optic nerve of necturus. *Biophys. J.* **120** (15), 3008–3027.

https://doi.org/10.1017/jfm.2026.11820 Published online by Cambridge University Press